OPEN ACCESS

Extracting and Interpreting Electrochemical Impedance Spectra (EIS) from Physics-Based Models of Lithium-Ion Batteries

To cite this article: Huayang Zhu *et al* 2024 *J. Electrochem. Soc.* **171** 050512

Journal of The Electrochemical Society, 2024 **171** 050512

Extracting and Interpreting Electrochemical Impedance Spectra (EIS) from Physics-Based Models of Lithium-Ion Batteries

Huayang Zhu,[1] Tyler A. P. Evans,[1] Peter J. Weddle,[2] Andrew M. Colclasure,[2] Bor-Rong Chen,[3] Tanvir R. Tanim,[3] Tyrone L. Vincent,[4] and Robert J. Kee[1]

[1]*Department of Mechanical Engineering, Colorado School of Mines, Golden, Colorado 80401, United States of America*
[2]*Center for Energy Conversion & Storage Systems, National Renewable Energy Laboratory, Golden, Colorado 80401, United States of America*
[3]*Energy Storage & Electric Transportation Department, Energy and Environmental Science and Technology, Idaho National Laboratory, Idaho Falls, Idaho, United States of America*
[4]*Department of Electrical Engineering, Colorado School of Mines, Golden, Colorado 80401, United States of America*

This paper implements a highly efficient algorithm to extract electrochemical impedance spectra (EIS) from physics-based battery models (e.g., a P2D model). The mathematical approach is different from how EIS is practiced experimentally. Experimentally, the voltage (current) is harmonically perturbed over a wide range of frequencies and the amplitude and phase shift of the corresponding current (voltage) is measured. The experimental approach can be implemented in simulation software, but is computationally expensive. The approach here is to determine locally linear state-space models from the full physical model. The four Jacobian matrices that are the basis of the state-space models can be derived by numerical differentiation of the physical model. The EIS is then extracted from the state-space model using computationally efficient matrix-manipulation techniques. The algorithm can evaluate the full EIS at an instant in time during a transient, independent of whether the battery is in a stationary state. The approach is also able to separate the full-cell impedance to evaluate partial EIS, such as for a battery anode alone. Although such partial EIS is difficult to measure experimentally, the partial EIS provides valuable insights in interpreting the full-cell EIS.
 [DOI: 10.1149/1945-7111/ad4399]

revised manuscript received April 13, 2024. Published May 8, 2024.

This paper reports results in three interrelated areas. The first, and perhaps the most significant, concerns the development and demonstration of a computationally efficient algorithm to extract electrochemical impedance spectra (EIS) from a physics-based model. The paper also documents the pseudo-two-dimensional (P2D) model that is used as the basis for demonstrating the EIS-extraction algorithm. Finally, the paper shows that transient polarization measurements (i.e., voltage versus current) alone are not sufficient to uniquely establish physical parameters in Li-ion battery models. However, modeling polarization and EIS together can greatly assist the interpretation of experimental data.

Physics-based models may be written generally and solved as systems of coupled non-linear partial differential equations with algebraic constraints. The EIS algorithm begins by linearizing the physics-based model in a state-space representation. The battery performance (e.g., charge or discharge) is modeled with the full nonlinear model. The state-space linearization is accomplished at some instant in time (i.e., some particular state of the battery). The EIS can be extracted very efficiently through a series of matrix manipulations.[1] Moreover, by partitioning the state variables and matrices, the algorithm can evaluate the impedance contributions of individual processes (e.g., how the anode chemistry and transport contribute to the full EIS).

The paper illustrates the EIS extraction and application using a pseudo-two-dimensional (P2D) Li-ion battery model.[2–4] However, the approach is generally applicable to other electrochemical models that resolve voltage/current dynamics (e.g., a fuel-cell model[5–8]). The P2D model itself and the EIS extraction are computationally efficient and fast, typically requiring about one minute on a typical personal computer.

Electrochemical impedance.—Electrochemical impedance spectroscopy is a powerful, widely used, non-invasive technique that measures electrochemical system performance.[9–11] The impedance spectra can be used to characterize electrochemical and physical phenomena (i.e., ionic transport, solid-phase diffusion, charge-transfer process), and to identify and track internal degradation processes.[11–13] By applying a low-amplitude harmonic current (galvanostatic mode) or voltage (potentiostatic mode) signal over a range of frequencies, the impedance spectra can be obtained by measuring the amplitude and phase shift of the output voltage or current, respectively. Figure 1 illustrates the physical meaning of electrochemical impedance. As shown, a sinusoidal perturbation current is imposed and a sinusoidal voltage response is observed. The frequency-dependent impedance is then a representation of the changes in magnitude $|Z|$ and phase shift θ from the input/output sinusoids. This process is repeated for numerous frequencies to produce the impedance spectra, which are typically plotted as Nyquist (Fig. 1b) or Bode formats.

Equivalent circuit models.—Equivalent-circuit representations are widely used to interpret the measured EIS. The equivalent circuits typically use a combination of electrical circuit components, such as resistors and capacitors, to describe the relationship between the input current and voltage response.[14] Although equivalent-circuit analysis is well established, there is always some ambiguity associated with assigning specific chemical and physical meanings to the equivalent-circuit elements.[9,15,16] In other words, for example, it can be difficult to directly associate an equivalent resistor or capacitor to a physical parameter such as a charge-transfer rate constant or an ion diffusion coefficient.

By contrast with equivalent-circuit models, physics-based models consider the coupled physicochemical processes and incorporate chemical and physical parameters directly, thus serving as a good foundation for quantifying the influences of contributing processes to the EIS. Most models involve numerous empirical functions and parameters that can be adjusted to fit measured behaviors. In addition to measured polarization behaviors (charge/discharge curves), EIS provides more and different data, which help establish the fitting of needed physical parameters.

Pseudo two-dimensional models.—Beginning in around 1993, Newman and colleagues developed a computational approach, which is usually called a pseudo-two-dimensional (P2D) model.[2] Over the years, there have been many adaptions and implementations of the

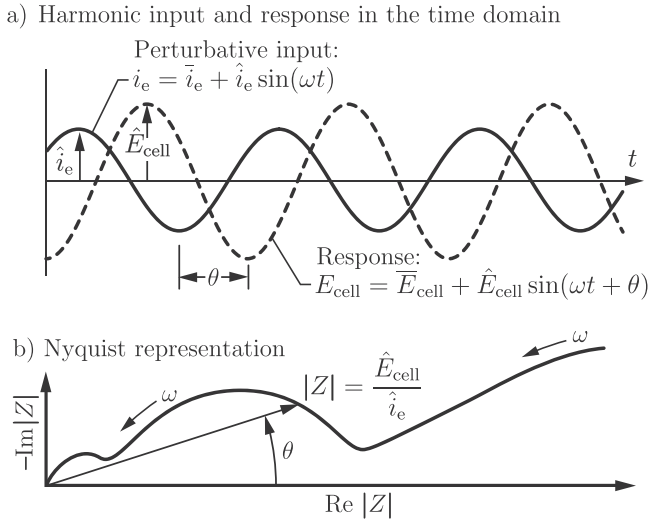

Figure 1. Electrochemical impedance extraction technique using harmonic perturbations. (a) Harmonic input perturbative current and voltage response in the time domain. (b) Nyquist response of the system.

general approach.[2–4] These models consider Li intercalation within the solid electrode phases as well as Li-ion transport within organic-solvent electrolyte phases. The P2D models are mathematically systems of coupled nonlinear partial differential-algebraic equations that must be solved computationally. As such, solving the P2D models is much more complex than solving equivalent-circuit models. Nevertheless, the model formulations and computational algorithms are well established and can usually be solved with only a few minutes on a personal computer. The objective herein is to develop similarly efficient algorithms to extract the EIS.

Alternative EIS approaches.—Both analytical and numerical approaches have been developed to extract the impedance spectra from P2D models. The analytical solutions are obtained in the frequency domain after linearization and using Laplace/Fourier transformations of the coupled transient nonlinear partial differential equations.[13,17–27] Because deriving the analytical solution is complex and tedious, different levels of simplification of the P2D models are generally applied. These analytical approaches are primarily concerned with the linear (first-order) system response, but recently efforts are underway to study higher-order frequency responses to uniquely identify internal parameters that were previously undetectable.[18,24] The numerical solutions are based on directly solving the P2D models in the time domain with a small sinusoidal, pulse, or step-change function of current or voltage input signal.[28–36]

Harmonic-perturbation algorithms can only evaluate the impedance spectra at the frequency of the perturbation, which is computationally expensive to evaluate a full EIS over wide frequency ranges. Computationally, it is greatly more efficient to use step-change perturbations (e.g., for current) and observe transient relaxations (e.g., voltage). Because the computational solution (i.e., the relaxation response) can be modeled very accurately, it is possible to recover the EIS from only a few perturbations.[30,33,37] However, as an inherently nonlinear and time-varying electrochemical system, the lithium-ion battery is charging (or discharging) after applying a step change in voltage or current. Thus state-of-charge varies while observing the transient relaxation. Ideally, the EIS should be measured and interpreted at a particular SOC under conditions of stability, causality, and linearity. So, to model the EIS the relaxation times must be short compared to the total discharge time, such that the SOC variations are small. However, very long relaxation times are required to capture very low frequency spectra, possibly leading to reduced accuracy or compromised meaning of the EIS.

In contrast to the small-perturbation algorithms, the present approach does not directly require evaluating a transient response. Rather, Jacobian matrices are evaluated computationally via finite differences from the physical model at some particular state (e.g., state of charge). The model would typically be run transiently and then relaxed to an equilibrium to achieve the particular state where the EIS is to be evaluated.

P2D Model

This Section documents the pseudo-two-dimensional (P2D) that is used in the present paper. Although all P2D models are structurally and computationally similar, there are numerous variations in particular implementations. The Appendix provides further details about specific parameters for a particular graphite-NMC532 battery.

Electrolyte Li^+ transport.—The mass conservation for the lithium-ion C_{Li^+} transport in the electrolyte (solvent) phase of the porous electrode and separator can be represented as

$$\frac{\partial \varepsilon_{el} C_{Li^+}}{\partial t} + \nabla \cdot \mathbf{J}_{Li^+} = \dot{r}_{Li^+}, \qquad [1]$$

where ε_{el} is the volume fraction of the electrolyte phase, $\dot{r}_{Li^+}$ is the net Li^+ production/consumption rate via charge-transfer reactions. The lithium-ion transport molar flux $\mathbf{J}_{Li^+}$ can be represented as

$$\mathbf{J}_{Li^+} = -D_{Li^+}\left(1 - \frac{\partial \ln C_0}{\partial \ln C_{Li^+}}\right)\nabla C_{Li^+} + \frac{t_+^\circ}{z_+ \nu_+ F}\mathbf{i}_{el}, \qquad [2]$$

where C_0 is the molar concentration of solvent in the electrolyte phase, which is usually assumed not to be a function of lithium-ion concentration C_{Li^+}. The Li^+ stoichiometric coefficient $\nu_+ = 1$ and charge number $z_+ = 1$ are taken for the $LiPF_6$ salt. The Li^+ effective diffusivity and transference number in the electrolyte are represented as D_{Li}^+ and t_+°, respectively.[38] F is the Faraday constant.

Current density and charge conservation.—The current density in the electrolyte phase $\mathbf{i}_{el}$ under the gradients of electric potential Φ_{el} and lithium-ion molar concentration C_{Li^+} can be expressed as,[39]

$$\mathbf{i}_{el} = -\sigma_{el}\nabla\Phi_{el} + \frac{2RT}{F}\sigma_{el}\mathscr{V}(1 - t_+^\circ)\nabla \ln C_{Li^+}, \qquad [3]$$

where σ_{el} is the effective conductivity of the lithium ion in the electrolyte. The thermodynamic factor $\mathscr{V}$ of the non-ideal electrolyte is defined as

$$\mathscr{V} = 1 + \frac{\partial \ln f_\pm}{\partial \ln C_{Li^+}}, \qquad [4]$$

where $f_\pm$ is the mean molar activity coefficient of the electrolyte.

The current density in the solid phase of the electrode (cathode or anode) $\mathbf{i}_{ed}$ under the gradient of the electrode-phase potential Φ_{ed} is represented using the Ohm's law as

$$\mathbf{i}_{ed} = -\sigma_{ed}\nabla\Phi_{ed}, \qquad [5]$$

where σ_{ed} is the effective conductivity of the electrode's solid phase.

Charge conservation within the electrode and electrolyte phases can be expressed as

$$\frac{\partial q_{ed}}{\partial t} + \nabla \cdot \mathbf{i}_{ed} = -F\dot{r}_{Li^+}, \qquad [6]$$

$$\frac{\partial q_{el}}{\partial t} + \nabla \cdot \mathbf{i}_{el} = +F\dot{r}_{Li^+}. \qquad [7]$$

where the local charge density due to the double-layer capacitance C_{dl} at the electrode-electrolyte interfaces can be represented as

$q_{ed} = -q_{el} = A_s C_{dl}(\Phi_{ed} - \Phi_{el})$, and A_s is the specific surface area of the active electrode per unit volume of the composite electrode.

Porous transport coefficients.—The effective transport properties within the porous electrode structure and separator (i.e., diffusivity D_m and conductivity σ_m) are related to the intrinsic properties using a Bruggeman factor as

$$\sigma_m = \sigma_m^{\circ}\varepsilon_m^{p_m}, \quad D_m = D_m^{\circ}\varepsilon_m^{p_m}, \tag{8}$$

where ε_m are the volume fractions, and p_m is the Bruggeman factor.

Lithium transport in electrode particles.—Unlike a typical P2D model, the present model accommodates particle size distribution within the electrode. The multiple electrode particle model accounts for the variation of particle radii, properties, and contact resistances within the electrodes. Because it is computationally inefficient to consider all the particles, the particles are normally regrouped into several sets with appropriate probability distribution.[40] Additionally, it is assumed that all the active electrode materials are exposed to the same electronic and ionic environment such that the local variations of the solid-phase and liquid-phase electric potentials as well as the species concentration in the electrolyte among the particles are neglected.

Mass conservation for intercalated lithium transport within the active spherical solid-phase particles at a given location can be represented as

$$\frac{\partial C_{Li,p}}{\partial t} + \nabla\cdot\mathbf{J}_{Li,p} = 0, \tag{9}$$

where $C_{Li,p}$ is the intercalated Li concentration in the pth particle. The index p denotes properties and fluxes associated with a specific particle radius within the particle size distribution. The lithium diffusive flux $\mathbf{J}_{Li,p}$ can be represented using the Fick's law as

$$\mathbf{J}_{Li,p} = -D_{Li,p}\nabla C_{Li,p}, \tag{10}$$

where $D_{Li,p}$ are the diffusion coefficients of the Li within representative electrode particles. On the particle surfaces, the Li flux within the particle is balanced by the charge transfer rate as

$$\mathbf{n}\cdot\mathbf{J}_{Li,p} = -\dot{s}_{Li^+,p}, \tag{11}$$

where $\dot{s}_{Li^+,p}$ denotes Li^+ production rate due to the charge transfer reactions on pth particle surface.

The overall Li^+ production rate $\dot{r}_{Li^+}$ of all the particles can be represented as

$$\dot{r}_{Li^+} = \varepsilon_{ed}\frac{\sum_p n_p A_p \dot{s}_{Li^+,p}}{\sum_p n_p V_p} = \varepsilon_{ed}\sum_p \frac{A_p}{V_p}\phi_p \dot{s}_{Li^+,p}, \tag{12}$$

where n_p, A_p, and V_p are the number density, surface area, and volume of pth particle, respectively. ϕ_p is the volume fraction of pth particle with respect to the total active material volume as

$$\phi_p = \frac{n_p V_p}{\sum_p n_p V_p} = \frac{f_p V_p}{\sum_p f_p V_p}, \tag{13}$$

where f_p is the particle number distribution. The specific surface area A_s of the active electrode per unit volume of the composite electrode can be expressed as

$$A_s = \varepsilon_{ed}\frac{\sum_p n_p A_p}{\sum_p n_p V_p} = \varepsilon_{ed}\sum_p \phi_p \frac{A_p}{V_p}. \tag{14}$$

Charge transfer.—Considering a single charge-transfer reaction at the electrode-electrolyte interfaces

$$Li(ed) \rightleftharpoons Li^+(el) + *\,(ed) + e^-(ed), \tag{15}$$

the charge-transfer reaction rates are represented using the Butler–Volmer formulation as

$$i_{BV} = i_0\left[\exp\left(\frac{\alpha_a F\eta_{act}}{RT}\right) - \exp\left(-\frac{\alpha_c F\eta_{act}}{RT}\right)\right], \tag{16}$$

where i_{BV} is the faradaic current density, i_0 is the exchange current density, and α_a and α_c are the anodic and cathodic symmetry factors, respectively. The Faraday constant is F, the gas constant is R, and the temperature is T. The overpotential η_{act} is defined as $\eta_{act} = E - E^{eq}$ where $E = \Phi_{ed} - \Phi_{el}$ is the potential difference between the electrode phase Φ_{ed} and electrolyte phase Φ_{el}, and E^{eq} is the equilibrium electric-potential difference. The exchange current density i_0 depends on the local concentrations of Li^+ within the electrolyte C_{Li^+} and intercalated Li within the electrode at the electrode-electrolyte interfaces C_{Li} as

$$i_0 = k_r F C_{Li^+}^{\alpha_a}[C_{Li}^{max} - C_{Li}]^{\alpha_a} C_{Li}^{\alpha_c}, \tag{17}$$

where k_r is a temperature-dependent rate constant. Defining $\theta_{el} = C_{Li^+}/C_{Li^+}^{max}$, and $\theta_{ed} = C_{Li}/C_{Li}^{max}$, the exchange current density i_0 can be separated into three parts: the temperature-dependent part $i_T^* = k_r F (C_{Li^+}^{max})^{\alpha_a} C_{Li}^{max}$, the Li^+ concentration-dependent part $i_{Li^+}^* = \theta_{el}^{\alpha_a}$, and the Li concentration-dependent part $i_{Li}^* = (1-\theta_{ed})^{\alpha_a}\theta_{ed}^{\alpha_c}$. Thus, the exchange current density can be rewritten as the product of three factors,

$$i_0 = i_T^* i_{Li^+}^* i_{Li}^*. \tag{18}$$

The temperature-dependent parameter i_T^* can be expressed generally as

$$i_T^* = i_0^{\circ}\exp\left[-\frac{E_{Li}^{act}}{R}\left(\frac{1}{T} - \frac{1}{T_{ref}}\right)\right], \tag{19}$$

where E_{Li}^{act} is the activation energy, i_0° is the exchange current density parameter i_T^* at a reference temperature T_{ref}.

A charge-transfer resistance R_{ct} can be evaluated from the Butler–Volmer equation (Eq. 16) as

$$R_{ct}^{-1} = \frac{\partial i_{BV}}{\partial \eta_{act}} = \frac{i_0 F}{RT}\left[\alpha_a\exp\left(\frac{\alpha_a F\eta_{act}}{RT}\right) + \alpha_c\exp\left(-\frac{\alpha_c F\eta_{act}}{RT}\right)\right], \tag{20}$$

which depends on the exchange current density i_0 and the activation overpotential η_{act}. High exchange current density i_0 and high activation overpotential η_{act} lead to low charge-transfer resistance R_{ct}, which leads to small impedance arcs in a Nyquist representation.

The Butler-Volmer rate expression of Eq. 16 can be applied to estimate the charge-transfer reaction rate $i_{BV,p}$ on each electrode particle-electrolyte interface. And the Li^+ production rate $\dot{s}_{Li^+,p}$ on the pth particle surface can be related to $i_{BV,p}$ as $\dot{s}_{Li^+,p} = i_{BV,p}/F$.

Spatial Discretization and State-Space Model

Equations 1, 6, 7, and 9 form a coupled nonlinear system of partial differential-algebraic equations (DAE), which can be solved computationally to obtain spatial profiles of lithium ion concentration in the electrolyte phase C_{Li^+}, lithium concentrations within the electrode particles C_{Li}, and electrostatic potentials Φ_{ed} and Φ_{el}. The numerical algorithm generally follows the method-of-lines.[41,42] The spatial operators in Eqs. 1, 6, 7, and 9 are discretized using a conservative finite-volume formulation.

Transient terms in Eqs. 6 and 7 are due to the charge storage of the double layer at the electrode-electrolyte interface. If the double-layer capacitance within the electrodes is negligibly small, and there is no charge storage within the dense electrolyte, the transient term in the electric-potential equations can usually be neglected. In this case, the spatially discretized electric-potential equations become nonlinear algebraic-constraint equations.

However, it becomes important to consider the double-layer capacitance in the P2D model in studying the electrochemical impedance of the batteries. The summation of charge conservation equations in the electrode and electrolyte phases (Eqs. 6 and 7) leads to the following total charge conservation equation

$$\nabla \cdot (\mathbf{i}_{\mathrm{ed}} + \mathbf{i}_{\mathrm{el}}) = 0, \qquad [21]$$

in which the transient term and charge-exchange term do not appear. Therefore, the solution can be obtained alternatively by solving Eqs. 1, 6, 9, and 21.

Defining $\mathbf{i}_{\mathrm{el}}^{\mathrm{c}}$ as the part of current density in the electrolyte phase under the Li^+ concentration gradients as

$$\mathbf{i}_{\mathrm{el}}^{\mathrm{c}} = \frac{2RT}{F}\sigma_{\mathrm{el}}\,\mathscr{V}(1 - t_+^{\circ})\,\nabla \ln C_{\mathrm{Li}^+}, \qquad [22]$$

the total charge conservation equation (Eq. 21) can be rewritten as

$$-\nabla \cdot (\sigma_{\mathrm{ed}} + \sigma_{\mathrm{el}})\nabla\Phi_{\mathrm{el}} = \nabla \cdot \sigma_{\mathrm{ed}}\nabla(\Phi_{\mathrm{ed}} - \Phi_{\mathrm{el}}) - \nabla \cdot \mathbf{i}_{\mathrm{el}}^{\mathrm{c}}, \qquad [23]$$

which is a linear Poisson equation for Φ_{el} after the C_{Li^+} profiles are found from solving from Eq. 1 and the potential difference $(\Phi_{\mathrm{ed}} - \Phi_{\mathrm{el}})$ from solving Eq. 6. Thus, the spatially discretized electrostatic-potential equations (Eq. 23) are linear algebraic-constraint equations within the DAE setting (Eqs. 1, 6, 9, and 21).

After discretizing the spatial operators of the partial differential equations, the resulting system forms a system of nonlinear ordinary differential-algebraic equations, which can be expressed formally and compactly as

$$\mathbf{M}\,\frac{\partial \mathbf{x}}{\partial t} = \mathbf{f}(\mathbf{x}(t, \mathbf{p}), \mathbf{u}(t), t; \mathbf{p}), \qquad [24]$$

where $\mathbf{f}$ is a nonlinear function and $\mathbf{M}$ is typically referred to as the mass matrix. The vector $\mathbf{x}$ represents states, $\mathbf{u}$ represents inputs or actuation, $\mathbf{p}$ represents parameters, and t represents time. More specifically, the state vector $\mathbf{x}(t, \mathbf{p}) = (\mathbf{C}_{\mathrm{Li}^+}, \mathbf{C}_{\mathrm{Li}}, \mathbf{q}_{\mathrm{ed}}, \mathbf{\Phi}_{\mathrm{el}})$ is comprised of concentrations, charge densities, and electrostatic potentials. $\mathbf{C}_{\mathrm{Li}^+}$ represents concentrations of lithium ion within the electrolyte phase on a spatially discretized finite-volume grid, $\mathbf{C}_{\mathrm{Li}}$ represents all the lithium concentrations within the representative electrode particles, the vector $\mathbf{q}_{\mathrm{ed}}$ represents the local charge density q_{ed} at the electrode-electrolyte interfaces, and Φ_{el} represents the electric potentials Φ_{el} on the discretized finite-volumes. $\mathbf{u}(t)$ represents the external variables or input such as the cell potential $E_{\mathrm{cell}} = \Phi_{\mathrm{ed}}|_{\mathrm{cc}} - \Phi_{\mathrm{ed}}|_{\mathrm{ac}}$ or the net current I. The mass matrix $\mathbf{M}$ is a diagonal matrix that can be formally expressed as $\mathbf{M} = \mathrm{Diag}(\mathbf{I}_{C_{\mathrm{Li}^+}}, \mathbf{I}_{C_{\mathrm{Li}}}, \mathbf{I}_{q_{\mathrm{ed}}}, \mathbf{0}_{\Phi_{\mathrm{el}}})$, where $\mathbf{I}$ is the identity matrix. Because there are no time derivatives in the discretized Eq. 23 for Φ_{el}, the mass matrix elements for Φ_{el} are zero.

Equation 24 can be solved using a differential-algebraic (DAE) solver, such as Limex.[43] However, for specified spatial profiles of C_{Li^+}, C_{Li}, and q_{ed} Eq. 23 is linear and can be solved easily and efficiently. Thus, without the dependent variables Φ_{el}, $\mathbf{x}(t, \mathbf{p})$ becomes $\mathbf{x}(t, \mathbf{p}) = (\mathbf{C}_{\mathrm{Li}^+}, \mathbf{C}_{\mathrm{Li}}, \mathbf{q}_{\mathrm{ed}})$, $\mathbf{M} = \mathbf{I}$, and Eq. 24 becomes a regular system of ordinary differential equations. Usually, ordinary differential equations are easier to solve than DAEs.

The system of nonlinear ordinary differential equations (Eq. 24) is considered to be a nonlinear dynamic system in the control community.[44–46] The dependent variables $\mathbf{x}(t, \mathbf{p})$ are the state variables and the input variables $\mathbf{u}(t)$ are control variables. The model output or response can be represented using observation functions as

$$\mathbf{y}(t, \mathbf{p}) = \mathbf{g}(\mathbf{x}(t, \mathbf{p}), \mathbf{u}, t; \mathbf{p}), \qquad [25]$$

where the cell potential is an observed output or response $\mathbf{y}(t, \mathbf{p}) = E_{\mathrm{cell}}(t, \mathbf{p})$ if the input $\mathbf{u}(t) = I$ for the battery models. The coupled combination of the state equations of Eq. 24 and the observation equations (Eq. 25) forms a nonlinear state-space model.

Linear State-Space Model and EIS

The physics-based P2D model (i.e., Eqs. 1, 6, 7, and 9) and its spatial discretization in terms of state-space representation (Eqs. 24 and 25) are inherently nonlinear. To compute the linear response of the physics-based model with respect to a low-amplitude harmonic perturbation and therefore extract impedance spectra, the nonlinear state-space should be linearized at a certain time and state.

Consider an input $\mathbf{u}(t) = \bar{\mathbf{u}}$ as applied to the system of Eqs. 24 and 25. From some initial state, the system evolves to a state $\bar{\mathbf{x}}$ with observable $\bar{\mathbf{y}}$ at time $\bar{t}$. With respect to $\bar{\mathbf{u}}(\bar{t})$ at time $\bar{t}$, a small harmonic perturbation $\hat{\mathbf{u}}(t)$ may be added to the input such that $\mathbf{u}(t) = \bar{\mathbf{u}}(\bar{t}) + \hat{\mathbf{u}}(t)$ is applied to the nonlinear system for $t \geqslant \bar{t}$. Then, both the state variables and observations respond as $\mathbf{x} = \bar{\mathbf{x}}(\bar{t}, \mathbf{p}) + \hat{\mathbf{x}}(t, \mathbf{p})$ and $\mathbf{y} = \bar{\mathbf{y}}(\bar{t}, \mathbf{p}) + \hat{\mathbf{y}}(t, \mathbf{p})$. Assuming that the perturbation $\hat{\mathbf{u}}(t)$ is very small such that both $\hat{\mathbf{x}}(t, \mathbf{p})$ and $\hat{\mathbf{y}}(t, \mathbf{p})$ are also very small, the nonlinear systems of Eqs. 24 and 25 can be linearized with respect to $\bar{\mathbf{u}}(\bar{t})$, $\bar{\mathbf{x}}(\bar{t}, \mathbf{p})$, and $\bar{\mathbf{y}}(\bar{t}, \mathbf{p})$ as

$$\mathbf{M}\,\frac{\partial \hat{\mathbf{x}}(t, \mathbf{p})}{\partial t} = \mathbf{A}\,\hat{\mathbf{x}}(t, \mathbf{p}) + \mathbf{B}\,\hat{\mathbf{u}}(t), \qquad [26]$$

$$\hat{\mathbf{y}}(t, \mathbf{p}) = \mathbf{C}\,\hat{\mathbf{x}}(t, \mathbf{p}) + \mathbf{D}\,\hat{\mathbf{u}}(t), \qquad [27]$$

with $\hat{\mathbf{x}}(\bar{t}, \mathbf{p}) = \mathbf{0}$. The Jacobian matrices $\mathbf{A}$, $\mathbf{B}$, $\mathbf{C}$, and $\mathbf{D}$ at $\bar{\mathbf{u}}(\bar{t})$ and $\bar{\mathbf{x}}(\bar{t}, \mathbf{p})$ are defined as

$$\mathbf{A} = \frac{\partial \mathbf{f}}{\partial \mathbf{x}},\quad \mathbf{B} = \frac{\partial \mathbf{f}}{\partial \mathbf{u}},\quad \mathbf{C} = \frac{\partial \mathbf{g}}{\partial \mathbf{x}},\quad \mathbf{D} = \frac{\partial \mathbf{g}}{\partial \mathbf{u}}, \qquad [28]$$

which are called state-space matrices of the linear systems.

The Laplace transformations of the input perturbation $\hat{\mathbf{u}}(t)$, the state response $\hat{\mathbf{x}}(t, \mathbf{p})$, and the observation response $\hat{\mathbf{y}}(t, \mathbf{p})$ may be denoted $\mathbf{U}(s)$, $\mathbf{X}(s, \mathbf{p})$, and $\mathbf{Y}(s, \mathbf{p})$, respectively. Considering $\hat{\mathbf{x}}(\bar{t}, \mathbf{p}) = \mathbf{0}$, the Laplace transformation of Eq. 26 becomes

$$s\mathbf{M}\mathbf{X} = \mathbf{A}\mathbf{X} + \mathbf{B}\mathbf{U}, \qquad [29]$$

from which $\mathbf{X}$ can be evaluated as

$$\mathbf{X} = (s\mathbf{M} - \mathbf{A})^{-1}\mathbf{B}\mathbf{U}. \qquad [30]$$

The Laplace transformation of Eq. 27 can be expressed

$$\mathbf{Y} = \mathbf{C}\mathbf{X} + \mathbf{D}\mathbf{U} = [\mathbf{C}(s\mathbf{M} - \mathbf{A})^{-1}\mathbf{B} + \mathbf{D}]\mathbf{U} = \mathbf{G}\mathbf{U} \qquad [31]$$

with the transfer function $\mathbf{G}$ being defined as

$$\mathbf{G} = \mathbf{C}(s\mathbf{M} - \mathbf{A})^{-1}\mathbf{B} + \mathbf{D}. \qquad [32]$$

Considering the input $\mathbf{u}(t)$ is the current I, and the output $\mathbf{y}(t, \mathbf{p})$ is the cell potential E_{cell}, the transfer function can be represented as

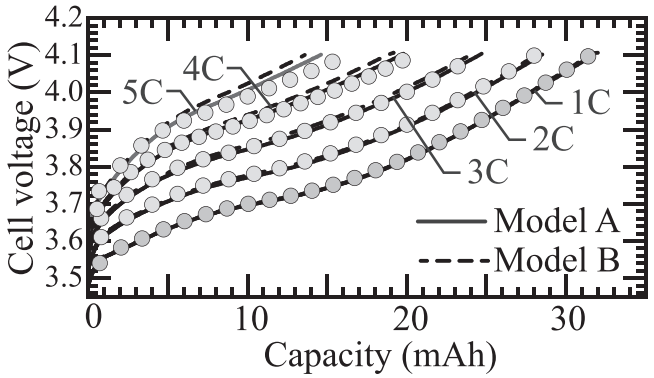

Figure 2. Comparison of the model predictions and measured polarization[4] for a P2D model with different parameters. The two models with different parameters are found to produce very similar polarization predictions. The operating temperature is nominally 30 °C and the model is operated isothermally.

Table I. Parameters for the LiC_6-NMC532 battery[4].

Anode parameters	
Thickness (μm)	70.0
Electrode volume fraction	0.5928
Electrolyte volume fraction	0.3450
Polymer phase volume fraction	0.0622
C_{Li}^{max} (mol cm^{-3})	30.53×10^{-3}
$C_{Li^+}^{0}$ (mol cm^{-3})	1.2×10^{-3}
Stoichiometry at 0% SOC	0.0700
Stoichiometry at 100% SOC	0.8434
Particle radius (μm)/Volume fraction	6.00/1.0
Bruggemann exponents (p_{ed}, p_{el})	2.0, 2.0
Charge-transfer coefficients (α_a,α_c)	0.5, 0.5
Cathode parameters	
Thickness (μm)	70.0
Electrode volume fraction	0.5131
Electrolyte volume fraction	0.3540
Polymer phase volume fraction	0.1329
C_{Li}^{max} (mol cm^{-3})	49.60×10^{-3}
$C_{Li^+}^{0}$ (mol cm^{-3})	1.2×10^{-3}
Stoichiometry at 0% SOC	0.8900
Stoichiometry at 100% SOC	0.3400
Particle radius (μm)/Volume fraction	1.5/0.75 2.5/0.25
Bruggemann exponents (p_{ed}, p_{el})	2.0, 2.0
Charge-transfer coefficients (α_a,α_c)	0.5, 0.5
Separator parameters	
Thickness (μm)	20.0
Electrolyte volume fraction	0.4000
$C_{Li^+}^{0}$ (mol cm^{-3})	1.2×10^{-3}
Bruggemann exponents (p_{el})	2.0

$$\mathbf{Z}(s, \mathbf{p}) = \mathbf{C}(s\mathbf{M} - \mathbf{A})^{-1}\mathbf{B} + \mathbf{D}, \qquad [33]$$

The electrochemical impedance can be obtained by setting $s = j\omega$, where ω is the desired frequency.

The impedance evaluation based on Eq. 33 involves only the manipulation of state-space matrices (i.e., **A**, **B**, **C**, **D**, and **M**) from the linear systems of Eqs. 26 and 27). Evaluating the matrices depends on the actuation $\bar{\mathbf{u}}(\bar{t})$ and state $\bar{\mathbf{x}}(\bar{t}, \mathbf{p})$ at time $\bar{t}$. The transient state $\mathbf{x}(t, \mathbf{p})$ is obtained by numerically solving the physics-based model or the nonlinear state-space model (i.e., Eq. 24) using DAE software such as LIMEX[43] or the ode15i function in MATLAB. The EIS extraction from the physics-based model can be accomplished at any instant time during the entire transient processes. The extraction can be implemented as a post-processing tool. Depending on the level of spatial discretization, and thus the size of the state-space matrices, each EIS extraction takes tens of seconds on a typical personal computer.

State-space matrices evaluation and partition.—The state-space derivatives **A**, **B**, **C**, and **D** can be approximated by the first-order finite differences, which is widely used in numerical mathematics, such as in implicit algorithms to solve nonlinear differential equations.[41] For example, consider how a small perturbation of the jth element x_j of the state vector **x** affects the ith element f_i of the function vector **f** at the state $\bar{\mathbf{x}}$. The Jacobian element $A_{i,j}$ of the matrix **A** is evaluated as

$$A_{i,j} = \frac{\partial f_i}{\partial x_j} \approx \frac{f_i(\bar{\mathbf{x}} + \Delta x_j \mathbf{e}_j, \bar{\mathbf{u}}, \bar{t}; \mathbf{p}) - f_i(\bar{\mathbf{x}}, \bar{\mathbf{u}}, \bar{t}; \mathbf{p})}{\Delta x_j}, \qquad [34]$$

where $\mathbf{e}_j$ is the jth unit vector of the state space, and the perturbation Δx_j is much smaller compared to $\bar{x}_j$. Typically, $\Delta x_j = \sqrt{u}\,\bar{x}_j$ where u is the computer's unit roundoff. Computational efficiency is usually achieved by sequentially perturbing elements of **x** and evaluating columns of the Jacobian.[42]

Reducing the rounding error of the finite-difference approximation is critical, especially at very low frequencies. Considering Eq. 33, it is evident that the approximation error ϵ in evaluating **A** should be much less than ω. If not, then the inverse $(s\mathbf{M} - \mathbf{A})^{-1}$ will be inaccurate. Evaluating the Jacobian derivatives using quadruple-precision (i.e., 128 bits with a precision of about 32 decimal digits) is found to produce reliable EIS even at very low frequencies.

The global state variables $\mathbf{x}(t, \mathbf{p})$ can be partitioned into three groups: $\mathbf{x}_a(t, \mathbf{p})$, $\mathbf{x}_e(t, \mathbf{p})$, and $\mathbf{x}_c(t, \mathbf{p})$, where $\mathbf{x}_a(t, \mathbf{p})$ represents all the state variables within the anode, $\mathbf{x}_e(t, \mathbf{p})$ represents all the state variables within the separator, and $\mathbf{x}_c(t, \mathbf{p})$ represents all the state variables within the cathode. The global state-space matrices **A**, **B**, **C**, and **D** can be correspondingly partitioned into three groups: $\mathbf{A}_m$, $\mathbf{B}_m$, $\mathbf{C}_m$, and $\mathbf{D}_m$ with $m = $ a, e, c. This enables evaluating the individual contributions $Z_m(s, \mathbf{p})$ associated with the anode, the separator, and the cathode to the total impedance based on the $\mathbf{A}_m$, $\mathbf{B}_m$, $\mathbf{C}_m$, and $\mathbf{D}_m$. The Jacobian of the observation with respect to the input is **D**. In this formulation, the observation is not directly related to the input. Thus, $\mathbf{D}_m = 0$.

To be concrete about computing times, consider an example. In the physics based P2D model, assume discretization with 20 finite volumes each for the anode, the separator, and the cathode. Further, consider 10 radial volumes for each of the representative electrode spheres within the anode and cathode. The compute time for a 5C charge using the P2D physics-based model is approximately 40 seconds. The compute time to evaluate any instance of the impedance spectra at some particular state is approximately 20 seconds. Of course, compute times depend upon the computer itself, the implementation language, functional dependencies of constitutive properties, mesh discretization, etc. In any case, the algorithm provides a highly efficient and effective means to extract EIS from a physics-based model.

P2D Models and Parameter Fitting

Pragmatically, as with most models, some empirical parameters and functions need to be adjusted such that the model's predictions are consistent with experimental observables. Parameters in P2D battery models are typically fit to, and "validated" with, polarization measurements at different charge/discharge rates. However, published literature reveals significantly different parameter sets for

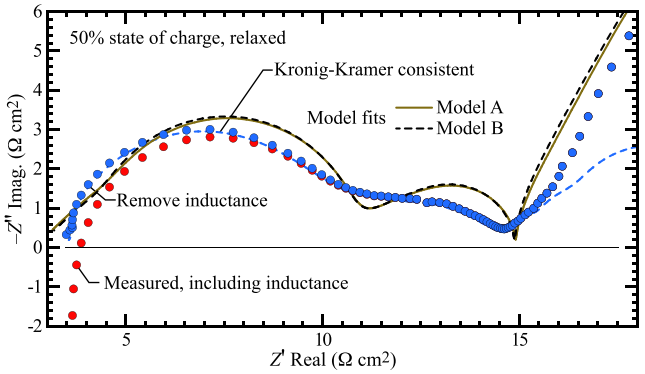

Figure 3. Comparison of the two model-predicted, KK-tested, and measured impedance spectra of a graphite-NMC532 battery at an open-circuit voltage of 3.7856 V and 30 °C. The EIS data is from Chen, et al.[49]

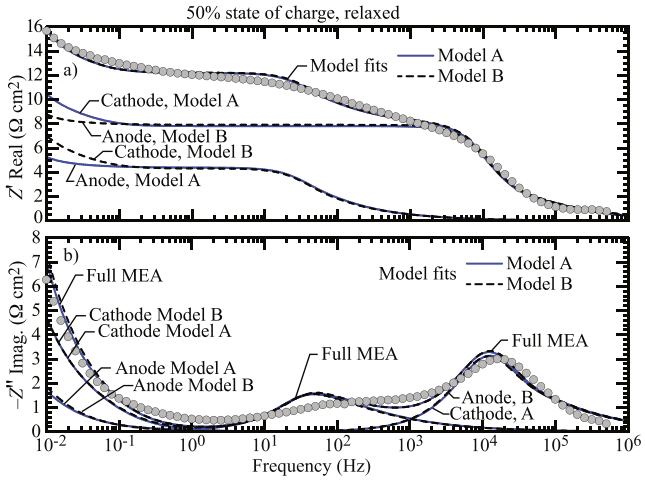

Figure 4. Comparison of the real and imaginary parts of the two model-predicted and measured EIS for the graphite-NMC532 battery. The graph also shows model-predicted anode and cathode contributions to the impedance. The model is operated isothermally at 30 °C.

Table II. Fitting parameters.

Parameters	Model A	Model B
$i^{\circ}_{0,a}$ (A cm^{-2})	9.8388×10^{-04}	4.2665×10^{-04}
$C_{dl,a}$ (F cm^{-2})	7.5658×10^{-05}	1.1225×10^{-07}
$i^{\circ}_{0,c}$ (A cm^{-2})	1.8177×10^{-04}	4.0947×10^{-04}
$C_{dl,c}$ (F cm^{-2})	3.3837×10^{-08}	2.2776×10^{-05}

nominally similar batteries.[47] Thus, it is apparent that polarization data alone is insufficient to uniquely establish needed parameters.[48] Augmenting polarization data with EIS measurements helps to constrain the parameter-fitting process. However, as discussed subsequently, even polarization and EIS data together are not sufficient to establish P2D parameters uniquely.

Figure 2 illustrates measured polarization behaviors for a graphite-NMC532 battery at five different charging rates.[4] The graphite anode is 70 μm thick, the NMC532 cathode is 70 μm thick, and the separator is 20 μm thick. The electrolyte is 1.2 M $LiPF_6$ in EC:EMC 3:7 (w:w). Table I summarizes other relevant physical parameters and the Appendix provides more detailed information about the battery.

Figure 3 illustrates the measured and modeled EIS at an open-circuit voltage of 3.78 V with the state of charge at 58.6%.[49] The

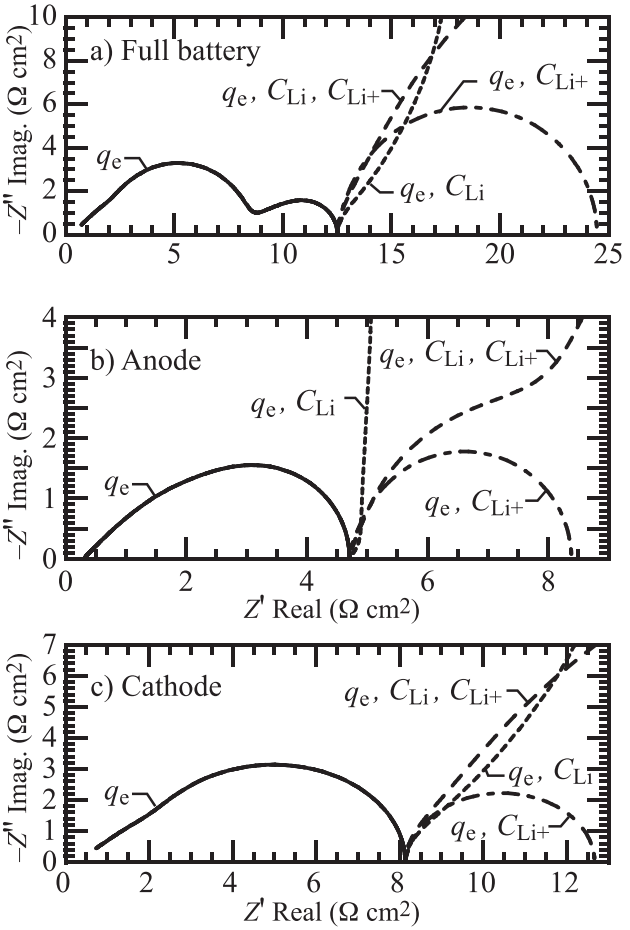

Figure 5. Comparison of impedance spectra of four combinations of state variables (i.e., charge-density q_e, lithium ion concentration C_{Li^+} in the electrolyte, and lithium concentration C_{Li} in the electrodes): 1) q_e; 2) q_e and C_{Li^+}; 3) q_e and C_{Li}; 4) q_e, C_{Li^+}, and C_{Li}. To maintain quantitative readability, note that the axis scales are different for each of the sub-plots.

measurements with the red markers include high-frequency inductive behavior. However, because the P2D models do not include inductive phenomena, the inductive contributions should be removed for the purposes of fitting other physical parameters. By fitting the measured EIS using an equivalent circuit, the high-frequency inductance is found to be $L \approx 2.14 \times 10^{-6}$ Ω s cm^2. The induction effects can be removed by subtracting the induction impedance $Z_L = j\omega L$ from the original measurement, leading to the EIS shown with blue markers.

Kramers–Konig compliance.—The real and imaginary impedance components as measured and reported may not be self consistent. A Kramers–Kronig test can be applied to determine the self consistency (i.e., determine the KK compliance).[50,51] The measured data shown in Fig. 3 are not KK compliant, especially at the lowest frequencies. The modified KK-compliant blue dashed line in Fig. 3 is determined by assuming the real impedance as measured and evaluating a KK-compliant imaginary impedance. It is common for reported battery EIS measurements at very low frequency to not satisfy fully the linearity, causality, and stationarity conditions required for Kramers–Kronig compliance.[50,51]

Fitting measured EIS.—The measured impedance in Fig. 3 shows three regions: high-frequency arc (i.e., 10^3 to 10^5 Hz), mid-frequency arc (i.e., 20 to 200 Hz), and a low-frequency tail (i.e., 0.01 to 1.0 Hz). The low-frequency impedance is attributed primarily to transport phenomenon. The high- and mid-frequency arcs may be

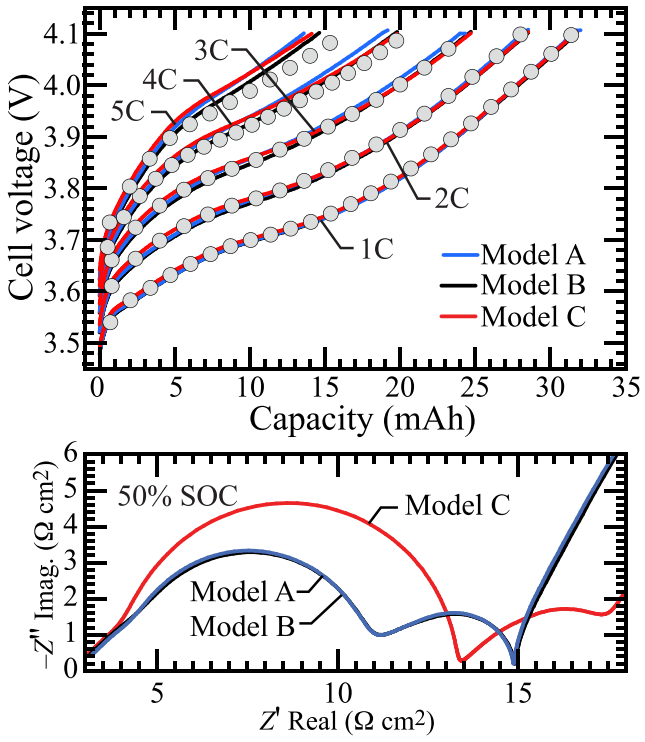

Figure 6. (a) Comparison of three model-predicted polarization curves against measurements of a LiC_6/NMC532 battery at five charging rates. (b) Comparison of the three model-predicted electrochemical impedance spectra at open-circuit voltage of 3.78 V and the state of charge of approximately 50%. The operating temperature is 30 °C.

attributed to charge-transfer kinetics. In this model, impedance contributions from the anode and cathode charge-transfer reactions are attributed to one of the two arcs. Thus, parameters associated with reaction kinetics may be tuned for each electrode to fit one of the arcs. In the present study, only four fitting parameters are considered: exchange current density $i^{\circ}_{0,a}$ within the anode, $i^{\circ}_{0,c}$ within the cathode, and double-layer capacitance $C_{dl,\ a}$ and $C_{dl,c}$ within the anode and cathode, respectively. Table II lists two different sets of parameters (denoted as Models "A" and "B"). Figure 3 shows that both models fit the measured impedance spectra reasonable well. Additionally, Fig. 2 shows Models A and B also predict the polarization charging behaviors well. At least two different P2D parameter sets are able to fit both polarization and limited EIS data well and the predictions from the two models are very close to each other. Both cannot be entirely physically correct, highlighting the parameter-uniqueness dilemma.

Figure 4 shows the real and imaginary components of impedance as a functions of frequency, comparing model predictions and measured (KK-complaint) results. The plot also shows the model-predicted anode and cathode impedance contributions from both Models A and B. For Model A, the cathode primarily contributes to the high-frequency arc and the anode primarily contributes to the mid-frequency arc. However, for Model B, the anode mainly contributes to the high-frequency arc while the cathode contributes primarily to the mid-frequency arc. For both models, lithium diffusion transport in the cathode particles primarily contributes to the low-frequency impedance.

Individual impedance contribution of states.—The P2D model has three state variables: profiles of local charge densities q_e, lithium-ion concentrations in the electrolyte C_{Li^+}, and lithium concentrations within the electrode particles C_{Li}. These are all coupled via charge-transfer processes. The state-space-model-based impedance algorithm enables evaluating the impedance of each

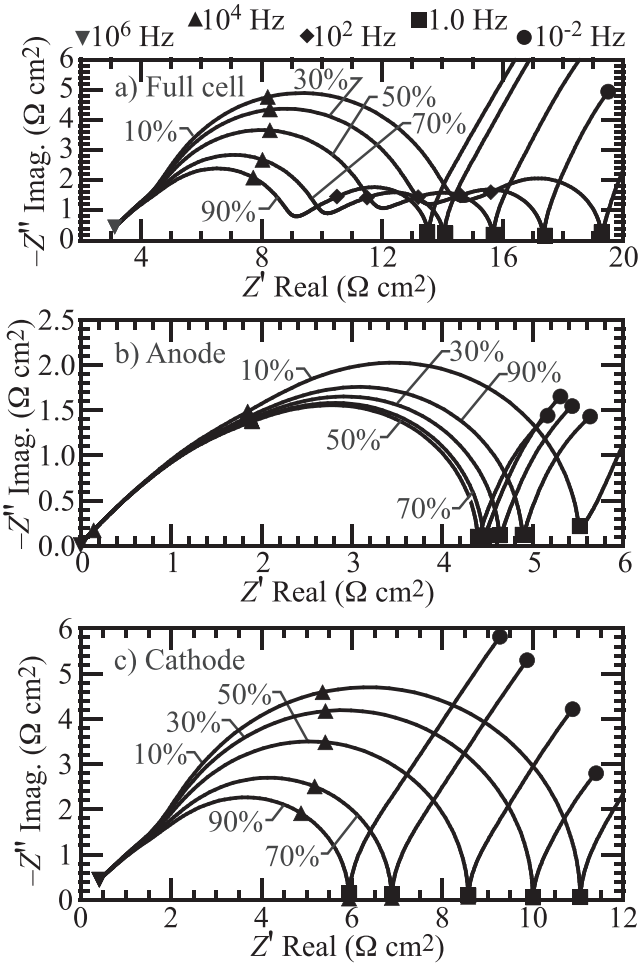

Figure 7. Model-predicted (Model A) anode and cathode contributions to full-cell EIS at five states of charge: 10%, 30%, 50%, 70%, and 90%. To maintain quantitative readability, note that the axis scales are different for each of the sub-plots. The markers identify selected frequencies on the Nyquist plots.

individual state variable or any combination thereof. Using the parameters of Model A, Fig. 5 compares the EIS of the combination of state variables in the anode, cathode, and the overall cell. Four combinations of state variables are considered: Case 1: q_e alone; Case 2: q_e and C_{Li^+}; Case 3: q_e and C_{Li}; and Case 4: q_e, C_{Li^+}, and C_{Li}.

As indicated in Fig. 5, the state variable q_e (Case 1), which represents the charge-storage capacity of the double layers at the electrode-electrolyte interfaces and involves directly the charge transport and transfer processes within the electrode, contributes to a single arc in the high-frequency region for both the anode and cathode. In combining q_e with C_{Li^+}, the mass transport of lithium ion C_{Li^+} in the electrolyte contributes to a low-frequency partial arc. In combining q_e with C_{Li}, the mass transport of lithium C_{Li} within the electrode particles contributes to a low-frequency tail. Because of the much slower transport of lithium C_{Li} within the electrode particles compared to lithium-ion C_{Li^+} transport within the electrolyte, the impedance contribution of C_{Li} transport dominates the low-frequency impedance.

Non-uniqueness of fitting parameters.—Figures 2 and 3 show that polarization measurements and EIS can be predicted equally well using two different sets of fitting parameters (Table II). By example, this is evidence that polarization and impedance measurements are insufficient to uniquely determine the physical and electrochemical parameters for P2D models. Further analysis and

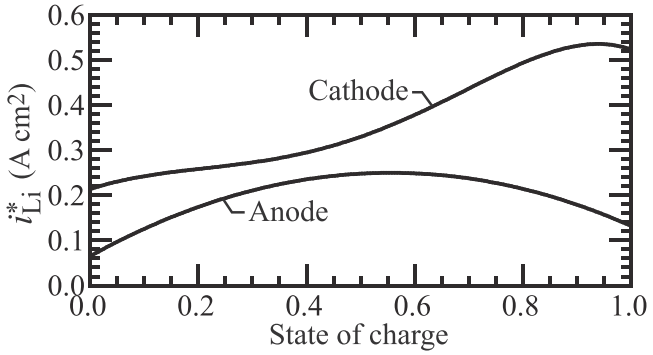

Figure 8. Lithium concentration-dependent part of exchange current density i^*_{Li} as functions of the state of charge using the Model A parameters.

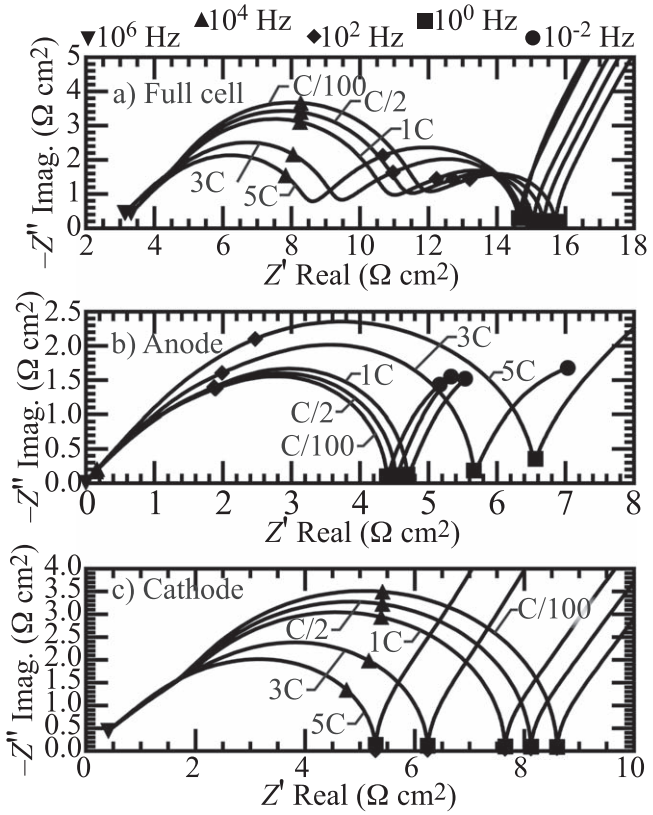

Figure 9. Comparison of the impedance spectra of the cell, anode, and cathode at the states of charge of 50% when the battery is charged from SOC = 0% at charging rates of 5C, 3C, 1C, C/2, and C/100. To maintain quantitative readability, note that the axis scales are different for each of the sub-plots. The markers identify selected frequencies on the Nyquist plots. Model A parameters are used.

discussion on parameter uniqueness using polarization and EIS data is available in Laue et al.[52]

Figure 6 includes results from another set of modeling parameters (Model C), which can predict the polarization curves well, but with EIS that is very different from the Model A and B impedance. Model C uses a single representative cathode particle size with a radius of 1.8 μm. The Bruggemann factors for both the electrode and electrolyte phases in the cathode are assumed to be 2.0, and the Bruggemann factor for the separator is assumed to be 2.4. The polarization curves are fitted first with the exchange-current density parameters: $i^\circ_{0,a} = 9.9780 \times 10^{-4}$ A cm^{-2}, and $i^\circ_{0,c} = 1.2900 \times 10^{-4}$ A cm^{-2}. Since fitting the polarization curves does not involve double-layer capacitances, the double-layer capacitances $C_{dl,a}$ and $C_{dl,c}$ required for predicting the measured impedance spectra are obtained by fitting the measured impedance by fixing the exchange current density parameters ($i^\circ_{0,a}$ and $i^\circ_{0,c}$). The best-fit double-layer capacitances are $C_{dl,a} = 5.3604 \times 10^{-3}$ F cm^{-2} and $C_{dl,c} = 2.6517 \times 10^{-8}$ F cm^{-2}. However, although fitting the polarization well, this parameter set does not predict the measured impedance. From this result, one concludes the exchange-current density impacts both polarization and EIS response. Exchange-current density is important when evaluating degradation behaviors, such as plating. For this reason, using both EIS and polarization to establish the parameter set is important for accurate model predictions.

Effects of State of Charge

Using the Model A fitting parameters, Fig. 7 illustrates how the impedance spectra depends on states of charge at 10%, 30%, 50%, 70%, and 90% SOC. These results assume that the battery is equilibrated at the specified SOC (i.e., state variables are spatially uniform). Figure 7a shows the model-predicted full-cell impedance, with Figs. 7b 7c showing the anode and cathode contributions. As the SOC increases from 10% to 90%, Fig. 7c shows that the impedance contributions from the cathode Z_c decrease. Because the cathode dominates the high-frequency response, the heights of the high frequency arcs in the full-cell and cathode EIS decrease monotonically as SOC increases (Figs. 7a and 7c). However, the anode contributions (Fig. 7b) are qualitatively different from the cathode behaviors as functions of SOC, and the high-frequency arc heights in the anode contributions are not monotonic with SOC.

Figure 8 shows the model-predicted lithium-concentration-dependent exchange current density i^*_{Li} as functions of the battery SOC. Because i^*_T and $i^*_{Li^+}$ (Eq. 18) do not change as functions of SOC under equilibrium conditions, the exchange current density i_0 and i^*_{Li} behave similarly as functions of SOC. Therefore, considering Eq. 20, when the SOC increases from 10% to 90%, i_0 for the cathode increases, leading to decreasing the charge-transfer resistance R_{ct} ($\eta_{act} = 0$ under the equilibrium condition). This leads to smaller impedance arcs (Fig. 7c) at higher SOC.

Figure 8 shows that the anode i^*_{Li} increases as SOC increases from 10% to 50%, but decreases when SOC increases further from 50% to 90%. Thus, the anode charge-transfer resistance is smallest at SOC $\approx$ 50%, causing the anode contribution to high-frequency arc to be lowest at SOC $\approx$ 50% (Fig. 7b). The same behavior contributes to mid-frequency arcs shifting to the left (Fig. 7a).

Dynamic Electrochemical Impedance

Lithium-ion batteries are intrinsically non-stationary and non-linear. However, EIS is typically measured and reported under stationary conditions (e.g., open circuit after relaxation to a stationary condition). Of course, EIS measurements are inherently transient, albeit using small transient perturbations around some nominally steady condition. Nevertheless, there is useful information that could be acquired by understanding impedance under non-stationary conditions. Such dynamic EIS can assist understanding and controlling degradation and aging mechanisms, states of health, electrode-electrolyte interfacial chemistry, etc. Several groups are developing both linear and nonlinear dynamic or in situ EIS techniques.[53–62] These dynamic EIS measurements are generally based on superimposing an alternating-current perturbation on a direct current during battery charging and discharging processes.

The present EIS-extraction algorithm can evaluate the impedance spectra from the physical model at any instant in time, enabling further interpretation of dynamic EIS measurements using the physics-based models. The following discussion considers a range of charging and discharging rates, evaluating EIS responses at a 50% SOC, but before relaxation to a stationary condition at the SOC.

In practice, measuring a full impedance spectrum (i.e., over large frequency ranges) during a transient is difficult. Especially at the low frequencies, the state of the battery changes during the course of

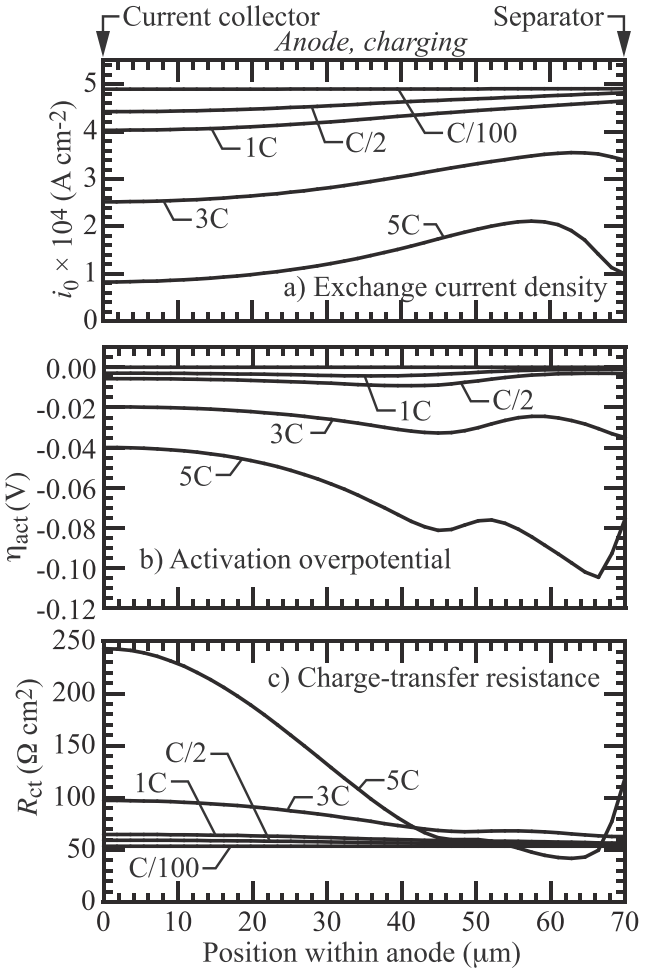

Figure 10. Comparison of the spatial profiles of i_0, η_{act} and R_{ct} within the anode at SOC = 50% when the battery is charged from SOC = 0% at five different charging rates: 5C, 3C, 1C, C/2, and C/100. Model A parameers are used.

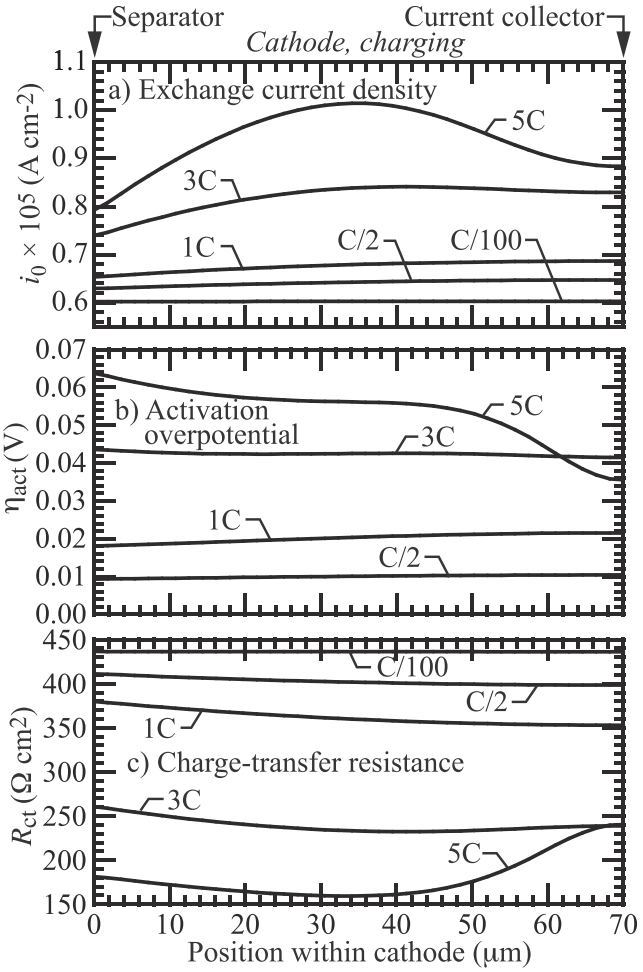

Figure 11. Comparison of the spatial profiles of i_0, η_{act} and R_{ct} within the cathode at SOC = 50% when the battery is charged from SOC = 0% at five different charging rates: 5C, 3C, 1C, C/2, and C/100.

measuring the impedance spectra. However, there is value in evaluating impedance at specific frequencies or over small frequency ranges. For example, Love et al.[63] report that state-of-health (SOH) can be predicted using measured impedance in frequency ranges around 300 Hz. The present algorithm, which predicts the instantaneous full EIS, assists in the physics-based interpretation of the specific-frequency impedance results. In other words, there is value in understanding the impedance in the vicinity of the single-point impedance diagnostic.

Effects of charge rate.—Using the parameters of Model A, Fig. 9 illustrates the effects of charging rate on the EIS. Consider that the battery is being charged from a 0% SOC to 50% SOC at five rates: 5C, 3C, 1C, C/2, and C/100. The EIS is evaluated immediately upon reaching 50% SOC, without waiting for the cell to equilibrate. Thus, the Li and Li^+ concentration profiles and electrostatic-potential profiles are not uniform throughout the cell. However, at very low charging rates (i.e., C/100), the profiles will be very close to being equilibrated. Although the model can evaluate the instantaneous EIS under these non-equilibrated conditions, there is no practical way to measure the full EIS experimentally.

Figure 9a shows the cell's predicted impedance spectra, with Figs. 9b and 9c showing the anode- and cathode-specific impedances. The height of the high-frequency arc (imaginary impedance) is highest at C/100 and lowest at 5C with the width of these arcs decreasing at higher charge rates. The mid-frequency arcs reveal different behavior, with the arc heights being greatest at 5C and lowest at C/100. Considering the anode and cathode contributions, it is evident that the cathode is most responsible for the full cell's high frequency behavior. The anode is largely responsible for the full cell's mid-frequency arcs. The trend seen in Fig. 4 corroborates this result. An impedance spectra, using Model B parameters, would show the anode is responsible for the cell's high-frequency impedance with the cathode responsible for the mid-frequency impedance.

Figure 10 shows spatial profiles of the anode's exchange current density i_0, activation energy η_{act}, and charge-transfer resistance R_{ct}. Figure 10a shows that the anode exchange current density i_0 at high charging rates is significantly smaller than it is at low charging rates. At high charge rates, the Li^+ concentration in the anode's electrolyte phase is reduced due to transport limitations in moving the Li^+ from the cathode to the anode. Because of lower Li^+ concentrations in the anode, the activation overpotential η_{act} must be greater (i.e., in Fig. 10b, larger negative) and the charge-transfer resistance R_{ct} higher. These effects are greatest near the current collector, where the Li^+ concentration is lowest. Figure 10c shows that the charge-transfer resistance R_{ct} increases as the charging rate increases. Thus, as Fig. 9b shows, the anode impedance increases with increasing charge rate, increasing the size of the mid-frequency arc (Fig. 9a).

Figure 11 compares spatial profiles of the cathode's i_0, η_{act}, and R_{ct} at different charge rates. Both the exchange current density i_0 and activation overpotential η_{act} increase as the charge rate increases, decreasing the charge-transfer resistance (Fig. 11c). In other words,

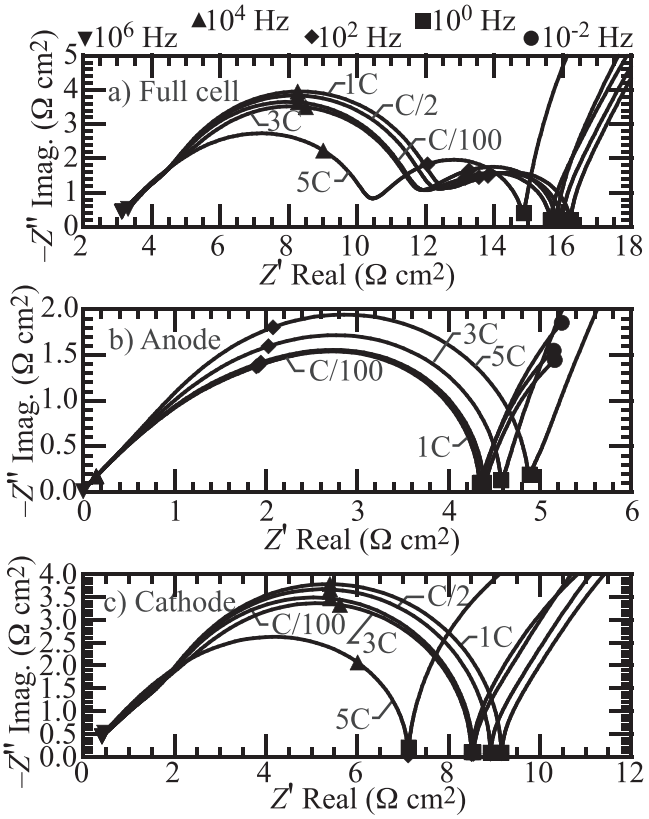

Figure 12. Impedance spectra of the full cell, anode, and cathode at 50% SOC when the battery is discharged from 100% SOC to 50% SOC at rates of 5C, 3C, 1C, C/2, and C/100. To maintain quantitative readability, note that the axis scales are different for each of the sub-plots. The markers identify selected frequencies on the Nyquist plots. Model A parameters are used.

high charge rates reduce the cathode impedance contribution, producing smaller high-frequency arcs (Fig. 9a).

Effects of discharge rate.—Continuing to use the parameters of Model A, Fig. 12 shows EIS during a discharge from 100% SOC to 50% SOC at five discharge rates. The EIS is evaluated immediately upon reaching 50% SOC. Thus, the cell is not equilibrated. However, at a very slow discharge rate of C/100, the state variables are nearly spatially uniform throughout the discharge transient. Figures 12b 12c show anode- and cathode-specific EIS behaviors. The high-frequency arcs of the full cell EIS are dominated by the cathode contributions while the anode contributions dominate the mid-frequency arcs of full-cell EIS. The results shown in Fig. 12 are corroborated by those shown in Fig. 4. These contributions are interchanged when using Model B parameters. The full cell EIS reveals some interesting behaviors. The height of the high-frequency arc is highest at 1C and lowest at 5C. However, the C/2 and C/100 high-frequency arcs lie within the 1C and 5C arcs (Fig. 12a).

Figure 13 shows the spatial profiles of exchange current density i_0, activation energy η_{act}, and charge-transfer resistance R_{ct} within the anode at 50% SOC at different discharging rate. As Fig. 13 illustrates, the exchange current density i_0 near the separator drops greatly at the high discharge rate of 5C due to the lower lithium concentrations at the particle surfaces. The charge-transfer rate near the separator is also small, increasing the charge-transfer resistance near the separator. The anode impedance contribution increases as the discharge rate increases (Fig. 12b), producing the relatively large mid-frequency arc at the highest discharge rate (Fig. 12a).

Figure 14 compares the spatial profiles of exchange current density i_0, activation energy η_{act}, and charge-transfer resistance R_{ct} within the cathode at 50% SOC in varying the discharging rate. Figure 14 shows that the exchange current density i_0 decreases as the

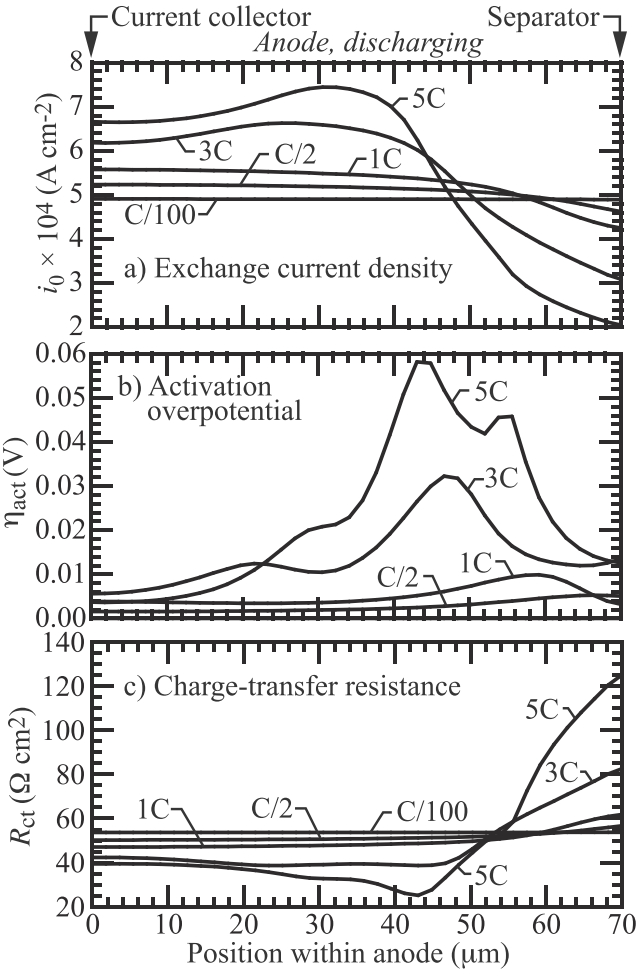

Figure 13. Spatial profiles of i_0, η_{act} and R_{ct} within the anode at 50% SOC when the battery is discharged from SOC = 100% at five different discharge rates: 5C, 3C, 1C, C/2, and C/100. Model A parameters are used.

discharging rate increases due to the lower Li^+ concentration in the electrolyte. However, the larger activation energy η_{act} is required to achieve the higher discharging rate. The opposite trend of i_0 and η_{act} in increasing the discharging rate leads to non-monotonic variation of the charge-transfer resistance. As indicated in Fig. 14c, R_{ct} near the separator increases when the discharging rate decreases from 5C to 1C, but decreases when the discharging rate further reduces to C/2, and C/100. Figure 12 shows that the cathode impedance increases when the discharging rate decreases from 5C to 1C, but decreases when the discharging rate increases to C/2 and C/100. Figure 12a shows the similar variation appears in the high-frequency arcs.

Summary and Conclusions

Electrochemical impedance spectra play important roles in assisting the design, characterization, and operation of electrochemical cells (e.g., batteries, fuel cells, electrolyzers, etc.). The measured EIS are typically interpreted in terms of equivalent-circuit models, with circuit elements being associated with physical behaviors. However, although very widely practiced and accepted, the circuit-to-physics association is indirect and heuristic. Physics-based models represent electrochemistry and transport processes in terms of conservation equations that can be posed as partial differential equations and solved computationally. These models directly incorporate physical and chemical processes. Several computational approaches have been developed to exercise the physics-based models to extract electrochemical impedance spectra. The present approach is computationally efficient and provides new avenues to assist EIS interpretation.

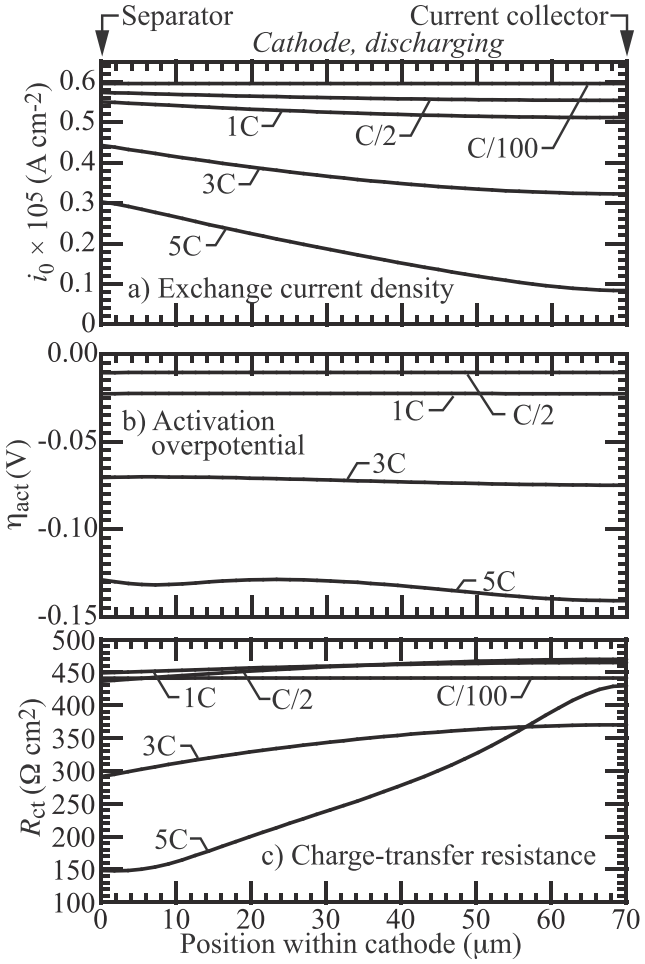

Figure 14. Spatial profiles of i_0, η_{act} and R_{ct} within the cathode at 50% SOC when the battery is discharged from SOC = 100% at five different discharge rates: 5C, 3C, 1C, C/2, and C/100. Model A parameters are used.

Models that solve transient conservation equations can be written abstractly as nonlinear state-space models. That is, simply put, the rates of change of state variables **x** depends upon nonlinear functions **f** of the states themselves, constitutive functions, physical parameters, and input actuations **u**. These models can be linearized by evaluating four Jacobian matrices that, for example, represent partial derivatives such as $\mathbf{A} = \partial\mathbf{f}/\partial\mathbf{x}$. Although the practitioner must have access to the model's source code, the Jacobian evaluation via numerical differentiation is efficient and straightforward. With the Jacobians in hand, evaluating the complex impedance (i.e., the EIS) is a matter of straightforward matrix manipulations. Although the mathematics of this process are well established, the authors are unaware of any prior application for batteries or other related electrochemical applications.

In addition to evaluating full EIS from the physics-based models, the algorithm can also to evaluate partial EIS. For example, the individual contributions of an anode or cathode alone can be evaluated. Although these partial contributions cannot be easily measured, understanding physics-specific contributions can assist interpretation of full impedance spectra.

Experimentally, EIS battery measurements are typically made around some steady-state operating point (e.g., open circuit at an equilibrium state of charge). The present algorithm, however, can evaluate the EIS at any instant during a transient, whether or not the battery is equilibrated. For example, assume a cell is fast charged to a specific SOC. Immediately upon reaching the SOC, there will be a non-equilibrated distribution of Li within the cell. Over time, at the fixed SOC, the battery will redistribute the Li to relax any concentration gradients within the electrode structures. Although the instantaneous EIS is not easily measured experimentally, valuable insights can be drawn from the model-predicted instantaneous, non-equilibrated, impedance spectra.

The combination of physics-based models and efficient EIS extraction can play a valuable role in evaluating physical parameters that are often included empirically in models. Physics-based models (e.g., P2D) are frequently validated using polarization measurements (voltage vs. current) alone. However, there can be significant ambiguity in the resulting best-fit parameters. Models that represent both polarization and EIS data can assist the establishment of reliable physics-based parameters.

Acknowledgments

The research at the Colorado School of Mines was supported by the Office of Naval Research via grant N00014-23-1-2694. This manuscript has been coauthored by the National Renewable Energy Laboratory operated by the Alliance for Sustainable Energy, LLC, for DOE under Contract No. DE-AC36-08GO28308, and the Battelle Energy Alliance, LLC, under Contract No. DE- AC07-05ID14517 for Idaho National Laboratory with the U.S. DOE. The views expressed in the article do not necessarily represent the views of the DOE or the U.S. Government. The United States Government retains and the publisher, by accepting the article for publication, acknowledges that the United States Government retains a non-exclusive, paid-up, irrevocable, worldwide license to publish or reproduce the published form of this manuscript, or allow others to do so, for United States Government purposes.

Appendix A. Properties of $LiPF_6$ in EC:EMC (3:7 w:w) Electrolyte

For $LiPF_6$ in EC:EMC 3:7 (w:w) electrolyte, the intrinsic lithium-ion diffusivity $D^{\circ}_{Li^+}$ (cm^2 s^{-1}) can be expressed as functions of T (K) and C_{Li^+} (M) as[64]

$$\log_{10}(D^{\circ}_{Li^+}) = \sum_{k=0}^{2} [D_{k,0} + D_{k,1}/(T - T_D)] C^k_{Li^+}, \qquad [A\cdot1]$$

where $T_D = -24.837\,63 + 64.073\,66 C_{Li^+}$, and the parameters $D_{k,0}$ and $D_{k,1}$ are listed in Table A·I.

Thermodynamic factor $\mathscr{V}$ is expressed as a function of T and C_{Li^+} (M) as

$$\mathscr{V} = 0.341 \exp(261.0/T) - 0.002\,25 \exp(1360.0/T) C_{Li^+} + 0.540 \exp(329.0/T) C^2_{Li^+}. \qquad [A\cdot2]$$

The intrinsic electric conductivity σ°_{el} (S m^{-1}) as a function of T and C_{Li^+} (M) is expressed as

$$\sigma^{\circ}_{el} = \sum_{\ell=1}^{4} \sum_{k=0}^{4} \sigma_{k\ell} T^k C^{\ell}_{Li^+}, \qquad [A\cdot3]$$

where $\sigma_{k\ell}$ are listed in Table A·II.

The transference number t°_{+} as functions of C_{Li^+} (M) and T (K) is expressed as

$$t^{\circ}_{+} = \sum_{\ell=0}^{2} \sum_{k=0}^{2} t_{k\ell} T^k C^{\ell}_{Li^+}, \qquad [A\cdot4]$$

where $t_{k\ell}$ are listed in Table A·III.

Table A·I. Parameters for diffusivity $D^{\circ}_{Li^+}$.

k	$D_{k,0}$	$D_{k,1}$
0	$-5.688\,226 \times 10^{-01}$	$-1.607\,003 \times 10^{+03}$
1	$-8.108\,721 \times 10^{-01}$	$+4.752\,914 \times 10^{+02}$
2	$-5.192\,312 \times 10^{-03}$	$-3.343\,827 \times 10^{+01}$

Table A·II. Parameters for electric conductivity σ°_{el}.

k	σ_{k1}	σ_{k2}
0	$+9.003410 \times 10^{+00}$	$-2.414638 \times 10^{+02}$
1	$-8.038545 \times 10^{-02}$	$+3.195295 \times 10^{-00}$
2	$+1.909446 \times 10^{-04}$	$-1.583677 \times 10^{-02}$
3		$+3.483638 \times 10^{-05}$
4		$-2.887587 \times 10^{-08}$
k	σ_{k3}	σ_{k4}
0	$+1.380\,976 \times 10^{+02}$	$-2.335\,671 \times 10^{+01}$
1	$-1.828\,064 \times 10^{-00}$	$+3.090\,003 \times 10^{-01}$
2	$+9.071\,155 \times 10^{-03}$	$-1.532\,707 \times 10^{-03}$
3	$-1.998\,760 \times 10^{-05}$	$+3.377\,143 \times 10^{-06}$
4	$+1.653\,786 \times 10^{-08}$	$-2.791\,965 \times 10^{-09}$

Table A·III. Parameters for transference number t°_{+}.

k	t_{k1}	t_{k2}	t_{k3}
0	$+3.091\,761 \times 10^{-01}$	$+1.777\,266 \times 10^{-01}$	$-3.881\,203 \times 10^{-02}$
1	$+6.389\,189 \times 10^{-04}$	$-8.682\,500 \times 10^{-04}$	$+2.077\,407 \times 10^{-04}$
2	$-6.766\,258 \times 10^{-07}$	$+1.161\,463 \times 10^{-06}$	$-2.876\,102 \times 10^{-07}$

Appendix B. Reversible Potentials of LiC_6 and NMC532

The open-circuit potential of the graphite anode E^{eq}_n is fitted as a function of $\theta_n = C_{Li}/C^{max}_{Li,\,LiC_6}$ as[64]

$$E^{eq}_n = \mathscr{E}_1 + (\mathscr{E}_2 - \mathscr{E}_1)/\mathscr{H}, \qquad [B\cdot1]$$

where

$$\mathscr{E}_1 = \mathscr{E}_0 + \sum_{k=1}^{8} \alpha_k \tanh(\theta_n + \beta_k)/\gamma_k, \qquad [B\cdot2]$$

$$\mathscr{E}_2 = \sum_{k=0} \xi_k \theta^k_n, \qquad [B\cdot3]$$

$$\mathscr{H} = 1.0 + \exp\left[-\zeta^*(\theta_n - \theta_0)\right], \qquad [B\cdot4]$$

with the parameters of $\mathscr{E}_0 = 0.659\,473\,500\,484\,747$, $\zeta = 100.0$, $\theta_0 = 1.029\,562\,032\,151\,98$. The parameters α_k, β_k, γ_k, and ξ_k are listed in Table B·I.

The open-circuit potential of NMC532 is fitted as a function of $\theta_p = C_{Li}/C^{max}_{Li,NMC}$ as[64]

Table B·I. Parameters for equilibrium potential E^{eq}_n of LiC_6.

k	α_k	k	β_k
1	$-1.05942335557277 \times 10^{-02}$	1	$-1.45370842560956 \times 10^{-02}$
2	$2.44361520308711 \times 10^{-02}$	2	$-5.46426136995040 \times 10^{-01}$
3	$-1.63752078805381 \times 10^{-02}$	3	$-5.63902501447549 \times 10^{-01}$
4	$-6.54236562289641 \times 10^{-02}$	4	$-5.96037052423359 \times 10^{-01}$
5	$-4.17322605929349 \times 10^{-02}$	5	$-1.78767058786864 \times 10^{-01}$
6	$-4.79217816384689 \times 10^{-01}$	6	$3.84570785201182 \times 10^{-03}$
7	$-4.36429392407499 \times 10^{-02}$	7	$-9.44923189331833 \times 10^{-02}$
8	$-8.24116639676041 \times 10^{-02}$	8	$-7.74668578957223 \times 10^{-02}$
k	γ_k	k	ξ_k
1	$9.089\,868\,397\,988\,61 \times 10^{-05}$	0	$-5.037944982759270 \times 10^{+01}$
2	$6.270\,508\,166\,379\,02 \times 10^{-01}$	1	$-1.228217254296760 \times 10^{+01}$
3	$7.053\,886\,409\,518\,52 \times 10^{-02}$	2	$-6.906367679257650 \times 10^{+01}$
4	$1.409\,966\,536\,648\,62 \times 10^{+00}$	3	$+3.437968012320620 \times 10^{+00}$
5	$7.693\,844\,911\,793\,47 \times 10^{-02}$	4	$+3.322960033709470 \times 10^{+01}$
6	$4.112\,633\,446\,959\,46 \times 10^{-02}$	5	$+5.913206621637760 \times 10^{+01}$
7	$-2.04677601257078 \times 10^{-02}$	6	$+1.233160814852810 \times 10^{+02}$
8	$3.593\,817\,905\,677\,97 \times 10^{-02}$	7	$+8.252008712749000 \times 10^{+01}$
		8	$-1.731504647676420 \times 10^{+02}$

Table B·II. Parameters for OCV of NMC532.[64]

k	a_k	k	a_k
1	$-5.57319176272331 \times 10^{-4}$	3	$4.148209275061330 \times 10^{1}$
2	$6.56024084265969 \times 10^{0}$		
k	b_k	k	b_k
0	$5.31473563300030 \times 10^{0}$	8	$-1.07437433318619 \times 10^{4}$
1	$-4.15827660360906 \times 10^{0}$	9	$-2.05780887352635 \times 10^{3}$
2	$2.72340921804213 \times 10^{1}$	10	$1.26563097851240 \times 10^{4}$
3	$-2.72485166844578 \times 10^{2}$	11	$-1.57109426436509 \times 10^{3}$
4	$1.19022342119331 \times 10^{3}$	12	$-1.45574206229136 \times 10^{4}$
5	$-2.07376554757481 \times 10^{3}$	13	$1.31765754448427 \times 10^{4}$
6	$-8.29790460410703 \times 10^{2}$	14	$-3.64011769200149 \times 10^{3}$
7	$8.69811275534872 \times 10^{3}$		

$$E^{eq}_p = a_1 \exp(a_2 \theta^{a_3}_p) + \sum_{k=0}^{14} b_k \theta^k_p, \qquad [B\cdot5]$$

where the parameters a_k and b_k are listed in Table B·II.

Appendix C. Electrode Diffusion D_{Li}

The temperature-depended diffusivity of lithium in the electrode particles D_{Li} can be generally expressed as

$$D_{Li} = D^{\circ}_{Li} \exp\left[-\frac{E^{Diff}_{Li}}{R}\left(\frac{1}{T} - \frac{1}{T_{ref}}\right)\right] \qquad [C\cdot1]$$

where E^{Diff}_{Li} is the activation energy, D°_{Li} is lithium diffusivity at the reference temperature of T_{ref}.

For the LiC_6 particles, $D^{\circ}_{Li,\,LiC_6} = 1.750 \times 10^{-13}$ m^2 s^{-1}, and $E^{Diff}_{Li,\,LiC_6} = 30.0$ kJ mol^{-1}. For NMC532, $D^{\circ}_{Li,\,NMC} = 1.125 \times 10^{\gamma}$ with $\gamma = \sum^{10}_{k=0} a_k \theta^k_p$, and the parameters a_k are listed in Table C·I, and the activation energy $E^{Diff}_{Li,\,NMC} = 30.0$ kJ mol^{-1}.

Table C·I. Parameters for diffusivity of NMC532.[64]

k	a_k	k	a_k
0	$-0.652609204639709 \times 10^{+02}$	6	$+0.105763602832900 \times 10^{+05}$
1	$+0.472370930424770 \times 10^{+03}$	7	$-0.833110410292107 \times 10^{+02}$
2	$-0.150243933907090 \times 10^{+04}$	8	$-0.486842026761136 \times 10^{+04}$
3	$+0.982489665964948 \times 10^{+03}$	9	$+0.239102672525997 \times 10^{+04}$
4	$+0.501627216777553 \times 10^{+04}$	10	$-0.250901084347927 \times 10^{+03}$
5	$-0.126832454834812 \times 10^{+05}$		

Appendix D. Charge Transfer Rates

For NMC532, the lithium concentration dependence of the exchange current density $i^*_{\text{Li, NMC}}$ can be fitted as function of θ_{ed} $(=\theta_{\text{p}})$ as

$$i^*_{\text{Li, NMC}} = \sum_{k=0}^{5} a_k \theta_{\text{ed}}^k, \qquad [\text{D·1}]$$

where a_k are listed in Table D·I. The parameters of temperature dependence of exchange current density are take as $i_0{}^\circ = 3.0$, and $E^{\text{act}}_{\text{Li, NMC}} = 30$ kJ mol^{-1}.

Table D·I. Parameters for exchange current density of NMC532.[64]

k	a_k	k	a_k
0	$-0.358529006582476 \times 10^{+01}$	3	$+0.124052469007304 \times 10^{+03}$
1	$+0.324976882173796 \times 10^{+02}$	4	$-0.752356714148880 \times 10^{+02}$
2	$-0.941657108128761 \times 10^{+02}$	5	$+0.165045282964129 \times 10^{+02}$

ORCID

Tyler A. P. Evans https://orcid.org/0000-0002-6303-4625
Peter J. Weddle https://orcid.org/0000-0002-1600-0756
Andrew M. Colclasure https://orcid.org/0000-0002-9574-5106
Tanvir R. Tanim https://orcid.org/0000-0002-1864-6868
Tyrone L. Vincent https://orcid.org/0000-0002-6921-8521
Robert J. Kee https://orcid.org/0000-0003-3930-4784

References

1. A. V. Oppenheim, A. S. Willsky, and S. H. Nawab, *Signals and Systems* (Prentice Hall, Upper Saddle River, NJ) 2 (1997).
2. M. Doyle, T. F. Fuller, and J. Newman, "Modeling of galvanostatic charge and discharge of the lithium/polymer/insertion cell." *J. Electrochem. Soc.*, **140**, 1526 (1993).
3. A. M. Colclasure and R. J. Kee, "Thermodynamically consistent modeling of elementary electrochemistry in lithium-ion batteries." *Electrochim. Acta*, **55**, 8960 (2010).
4. A. M. Colclasure, A. R. Dunlop, S. E. Trask, B. J. Polzin, A. N. Jansen, and K. Smith, "Requirements for enabling extreme fast charging for high energy density Li-ion cells while avoiding lithium plating." *J. Electrochem. Soc.*, **166**, A1412 (2019).
5. H. Zhu, R. J. Kee, V. M. Janardhanan, O. Deutschmann, and D. G. Goodwin, "Modeling elementary heterogeneous chemistry and electrochemistry in solid-oxide fuel cells." *J. Electrochem. Soc.*, **152**, A2427 (2005).
6. H. Zhu and R. J. Kee, "Modeling distributed charge-transfer processes in SOFC membrane electrode assemblies." *J. Electrochem. Soc.*, **155**, B715 (2008).
7. H. Zhu and R. J. Kee, "Modeling protonic-ceramic fuel cells with porous composite electrodes in a button-cell configuration." *J. Electrochem. Soc.*, **164**, F1400 (2017).
8. H. Zhu, A. Ashar, R. J. Kee, R. J. Braun, and G. S. Jackson, "Physics-based model to represent membrane-electrode assemblies of solid-oxide fuel cells based on gadolinium-doped ceria." *J. Electrochem. Soc.*, **170**, 104506 (2023).
9. D. D. Macdonald, "Reflections on the history of electrochemical impedance spectroscopy." *Electrochim. Acta*, **51**, 1376 (2006).
10. F. Ciucci, "Modeling electrochemical impedance spectroscopy." *Curr. Opin. Electrochem.*, **13**, 132 (2019).
11. N. Meddings et al., "Application of electrochemical impedance spectroscopy to commercial Li-ion cells: A review." *J. Power Sources*, **480**, 228742 (2020).
12. P. Iurilli, C. Brivio, and V. Wood, "On the use of electrochemical impedance spectroscopy to characterize and model the aging phenomena of lithium-ion batteries: a critical review." *J. Power Sources*, **505**, 229860 (2021).
13. A. Mallarapu, S. Santhanagopalan, W. Uno, Y. Kanai, Y. Uemura, R. Yagi, and S. Uchikoga, "Simulation of impedance changes with aging in lithium titanate-based cells using physics-based dimensionless modeling." *J. Electrochem. Soc.*, **170**, 090519 (2023).
14. E. Barsoukov and J. R. Macdonald, *Impedance Spectroscopy: Theory, Experiment, and Applications* (Wiley, Hoboken, NJ) (2018).
15. R. Xiong, J. Tian, H. Mu, and C. Wang, "A systematic model-based degradation behavior recognition and health monitoring method for lithium-ion batteries." *Appl. Energy*, **207**, 372 (2017).
16. A. Nenning, A. K. Optiz, T. M. Huber, and J. Fleig, "A novel approach for analyzing electrochemical properties of mixed conducting solid oxide fuel cell anode materials by impedance spectroscopy." *Phys. Chem. Chem. Phys.*, **16**, 22321 (2014).
17. K. Takano, K. Nozaki, Y. Saito, K. Jato, and A. Negishi, "Impedance spectroscopy by voltage-step chronoamperometry using the Laplace transform method in a lithium-ion battery." *J. Electrochem. Soc.*, **147**, 2930 (2000).
18. M. D. Murbach and D. T. Schwartz, "Extending Newman's pseudo-two-dimensional lihtium-ion battery impedance similuation approach to include non-linear harmonic response." *J. Electrochem. Soc.*, **164**, E3311 (2017).
19. J. P. Meyers, M. Doyle, R. M. Darling, and J. Newman, "The impedance response of a porous electrode composed of intercalation particles." *J. Electrochem. Soc.*, **147**, 2930 (2000).
20. M. Doyle, J. P. Meyers, and J. Newman, "Computer simulations of the impedance response of lithium rechargeable batteries." *J. Electrochem. Soc.*, **147**, 99 (2000).
21. M. Pathak, M. D. Murbach, C. Pathak, T.-J. Jang, Y. Qi, D. T. Schartz, and V. R. Subramanian, "Fast impedance simulation of lithium-ion bateries with pseudo-two dimensional electrochemical models." *J. Electrochem. Soc.*, **165**, A1324 (2018).
22. G. Sikha and R. E. White, "Analytical expression for the impedance response for a lithium-ion cell." *J. Electrochem. Soc.*, **155**, A893 (2008).
23. J. Huang and J. Zhang, "Theory of impedance response of porous electrodes: Simplifications, inhomogeneities, non-stationarities and applications." *J. Electrochem. Soc.*, **163**, A1983 (2016).
24. T. L. Kirk, A. Lewis-Douglas, D. Howey, C. P. Please, and S. J. Chapman, "Nonlinear electrochemical impedance spectroscopy for lithium-ion battery model parameterization." *J. Electrochem. Soc.*, **170**, 010514 (2023).
25. S. Devan, V. R. Subramanian, and R. E. White, "Analytical solution for the impedance of a porous electrode." *J. Electrochem. Soc.*, **151**, A905 (2004).
26. G. Sikha and R. E. White, "Analytical expression for the impedance response of an insertion electrode cell." *J. Electrochem. Soc.*, **154**, A43 (2007).
27. D. Gruet, B. Delobel, D. Sicsic, I. T. Lucas, and V. Vivier, "On the electrochemical impedance response of composite insertion electrodes–Toward a better understanding of porous electrodes." *Electrochim. Acta*, **295**, 787 (2019).
28. Y. Xie, J. Li, and C. Yuan, "Mathematical modeling of the electrochemical impedance spectroscopy in lithium ion battery cycling." *Electrochim. Acta*, **127**, 266 (2014).
29. J. Lück and A. Latz, "The electrochemical double layer and its impedance behavior in lithium-ion batteries." *Phys. Chem. Chem. Phys.*, **21**, 14753 (2019).
30. P. J. Weddle, R. J. Kee, and T. Vincent, "A stitching algorithm to identify wide-bandwidth electrochemical impedance spectra for Li-ion batteries uing binary perturbations." *J. Electrochem. Soc.*, **165**, A1679 (2018).
31. T. Söderström and P. Stoica, *System Identification* (Prentice-Hall, Inc.) (1988).
32. L. Ljung, *System Identification: Theory for the User* (Prentice Hall, Upper Saddle River, NJ) (1999).
33. H. Zhu, A. Krump, A. Leonide, E. Ivers-Tiffée, O. Deutschmann, and R. J. Kee, "A model-based interpretation of the influence of anode surface chemistry on solid oxide fuel cell electrochemical impedance spectra." *J. Electrochem. Soc.*, **159**, F255 (2012).
34. P. J. Weddle, "Developing and identifying physically based Li-ion battery models to inform real-time control applications." *PhD thesis*, Colorado School of Mines (2019).
35. G. L. Plett, "Extended Kalman filting for battery management systems of LiPB-based HEV battery packs: Part 2. Modeling and identification." *J. Power Sources*, **134**, 262 (2004).
36. P. J. Weddle, T. L. Vincent, A. La Rue, H. Zhu, and R. J. Kee, "Complex impedance of Li-ion-battery phase-transformation electrodes at history-dependent states of charge." *J. Electrochem. Soc.*, **166**, A2485 (2019).
37. W. G. Bessler, "Rapid impedance modeling via potential step and current relaxation simulations." *J. Electrochem. Soc.*, **154**, B1186 (2007).
38. S. C. DeCaluwe, P. J. Weddle, H. Zhu, A. M. Colclasure, W. G. Bessler, G. S. Jackson, and R. J. Kee, "On the fundamental and practicle aspects of modeling complex electrochemical kinetics and transport." *J. Electrochem. Soc.*, **165**, E637 (2018).
39. M. Doyle, J. Newman, A. S. Gozdz, C. N. Schmutz, and J. M. Tarascon, "Comparison of modeling predictions with experimental data from plastic lithium ion cells." *J. Electrochem. Soc.*, **143**, 1890 (1996).
40. T. L. Kirk, J. Evans, C. P. Please, and S. J. Chapman, "Modeling electrode heterogeneity in lithium-ion batteries:Unimodal and bimodal particle-size distributions." *SIAM J. Appl. Math.*, **82**, 625 (2022).

41. U. M. Ascher and L. R. Petzold, *Computer Methods for Ordinary Differential Equations and Differential-Algebraic Equations* (SIAM, Philadelphia, PA) (1998).
42. R. J. Kee, M. E. Coltrin, P. Glarborg, and H. Zhu, *Chemically reacting flow: Theory modeling and simulation.* (Wiley, Hoboken, NJ) 2nd ed. (2018).
43. P. Deuflhard, E. Hairer, and J. Zugck, "One-step and extrapolation methods for differential-algebraic systems." *Numer. Math.*, **51**, 501 (1987).
44. G. L. Plett, "Sigma-point Kalman filtering for battery management systems of LiPB-based HEV battery packs: Part 1: Introduction and state estimation." *J. Power Sources*, **161**, 1356 (2006).
45. H. Perez, X. Hu, S. Dey, and S. Moura, "Optimal charging of Li-ion batteries with coupled electro-thermal-aging dynamics." *IEEE Trans. Veh. Technol.*, **66**, 7761 (2017).
46. S. Mohan, Y. Kim, and A. G. Stefanopoulou, "Energy-conscious warm-up of li-ion cells from subzero temperatures." *IEEE Trans. Ind. Electron.*, **63**, 2954 (2016).
47. W. Li, U. Demir, D. Cao, D. Jöst, F. Ringbeck, M. Junker, and D. U. Sauer, "Data-driven systematic parameter identification of an electrochemical model for lithium-ion batteries with artificial intelligence." *Energy Storage Mater.*, **44**, 557 (2022).
48. D. Lu, M. S. Trimboli, and G. Plett, "Cell discharge testing to calibrate a positive-electrode open-circuit-potential model for lithium-ion cells." *J. Electrochem. Soc.*, **169**, 070524 (2022).
49. B. R. Chen, Y. R. Police, M. Li, P. R. Chinnam, T. R. Tanim, and E. J. Dufek, "A mathematical approach to survey electrochemical impedance spectroscopy for aging in lithium-ion batteries." *Front. Energy Res.*, **11**, 01 (2023).
50. B. A. Boukamp, "A linear Kronig-Kramers transform test for immittance data validation." *J. Electrochem. Soc.*, **142**, 1885 (1995).
51. M. Schönleber, D. Klotz, and E. Ivers-Tiffée, "A method for improving the robustness of linear Kramers-Kronig validity tests." *Electrochim. Acta*, **131**, 20 (2014).
52. V. Laue, F. Röder, and U. Krewer, "Practical identifiability of electrochemical P2D models for lithium-ion batteries." *J. Appl. Electrochem.*, **51**, 1253 (2021).
53. Z. Stoynov, B. Savova-Stoynov, and T. Kossev, "Non-stationary impedance analysis of lead/acid batteries." *Front. Energy Res.*, **30**, 275 (1990).
54. J. Huang, H. Ge, Z. Li, and J. Zhang, "Dynamic electrochemical impedance spectroscopy of a three-electrode lithium-ion battery during pulse charge and discharge." *Electrochim. Acta*, **176**, 311 (2015).
55. M. Itagaki, N. Kobari, S. Yotsuda, K. Watanabe, S. Kinoshita, and M. Ue, "In situ electrochemical impedance spectroscopy to investigate negative electrode of lithium-ion rechargeable batteries." *J. Power Sources*, **135**, 255 (2004).
56. M. Itagaki, K. Honda, Y. Hoshi, and I. Shitanda, "In-situ EIS to determine impedance spectra of lithium-ion rechargeable batteries during charge and discharge cycle." *J. Electroanaly. Chem.*, **737**, 78 (2015).
57. H. Watanabe, S. Omoto, Y. Hoshi, I. Shitanda, and M. Itagaki, "Electrochemical impedance analysis on positive electrode in lithium-ion battery with galvanostatic control." *J. Power Sources*, **507**, 230258 (2021).
58. M. Kuipers, P. Schröer, T. Nemeth, H. Zappen, A. Blömeke, and D. U. Sauer, "An algorithm for an online electrochemical impedance spectroscopy and battery parameter estimation: Development, verification and validation." *J. Energy Storage*, **30**, 101517 (2020).
59. X. Zhu, N. Hallemans, B. Wouters, R. Claessens, J. Lataire, and A. Hubin, "Operando odd random phase electrochemical impedance spectroscopy as a promising tool for monitoring lithium-ion batteries during fast charging." *J. Power Sources*, **544**, 231852 (2022).
60. N. Hallemans, W. D. Widanage, X. Zhu, S. Moharana, M. Rashid, A. Hubin, and J. Lataire, "Operando electrochemical impedance spectroscopy and its application to commercial li-ion batteries." *J. Power Sources*, **547**, 232005 (2022).
61. K. J. Szekeres, S. Vesztergom, M. Ujvári, and G. G. Láng, "Methods for the determination of valid impedance spectra in non-stationary electrochemical systems: Concepts and techniques of practical importance." *ChemElectroChem*, **8**, 1233 (2021).
62. J. D. Huang, "Elucidating Electrochemical Mechanisms with Accelerated Characterization and Relaxation Structure Analysis." *PhD thesis*, Colorado School of Mines (2023).
63. C. T. Love, M. B. V. Virji, R. E. Rocheleau, and K. E. Swider-Lyons, "State-of-health monitoring of 18 650 4S packs with a single-point impedance diagnostic." *J. Power Sources*, **266**, 512 (2014).
64. W. Mai, A. M. Colclasure, and K. Smith, "Model-instructed design of novel charging protocols for the extreme fast charging of lithium-ion batteries without lithium plating." *J. Electrochem. Soc.*, **167**, 080517 (2020).